Geochimica et Cosmochimica Acta 414 (2026) 169–190

Contents lists available at ScienceDirect

Geochimica et Cosmochimica Acta

journal homepage: www.elsevier.com/locate/gca

Experimental kinetic rate laws for aqueous pyrite reduction at underground hydrogen storage conditions (60–150 °C, up to 150 bar H_2)

Robin Hintzen [a,*], Roland Hellmann [b], Vladimir Roddatis [c], Julia van Winden [d], Laurent Truche [a,*]

[a] Université Grenoble Alpes, Institute for Earth Sciences (ISTerre), 1381 Rue de la Piscine, CS 40700, 38058 Grenoble CEDEX9, France
[b] Université Grenoble Alpes, CNRS, Institute for Earth Sciences (ISTerre), 1381 Rue de la Piscine, CS 40700, 38058 Grenoble CEDEX9, France
[c] GFZ Helmholtz Centre for Geosciences, Telegrafenberg, Potsdam 14473, Germany
[d] Shell Global Solutions International B.V., Carel van Bylandtlaan 16, 2596 HR The Hague, the Netherlands

ARTICLE INFO

Associate editor: Carl Steefel

Keywords:
Underground hydrogen storage
UHS
Pyrite
Hydrogen
H_2
Dissolution kinetics
H_2S
Sulfide
Pyrrhotite
Hydrothermal experiments
Redox reactions
Energy transition

ABSTRACT

The reaction kinetics of reductive pyrite (FeS_2) dissolution by H_2 is important to predict the long-term aqueous and gaseous sulfide release in underground hydrogen storage and other engineered subsurface sites. We investigated the rates of pyrite reduction based on sulfide formation as a function of temperature (60-150 °C), H_2 partial pressure (0-150 bar), and $pH_{in\ situ}$ (~ 4-10) in deoxygenated 0.03 M NaCl solutions. The experiments used natural pyrite powder (ø = 50-100 µm) and were run in hydrothermal batch reactors made of either titanium or Dursan®-coated 316L stainless steel. After experimental durations of ~ 700-900 h, dissolved $S^{-II}_{(aq)}$ concentrations measured by methylene blue spectrophotometry ranged from 10^{-5} to 10^{-3} M. Long-term pyrite dissolution and concomitant elevated $S^{-II}_{(aq)}$ concentrations were controlled by the formation of secondary pyrrhotite ($Fe_{1-x}S$) and magnetite (Fe_3O_4), which prevented the ion activity product of FeS_2 from achieving rapid saturation. Conversely, in the absence of pyrrhotite and magnetite precipitation, the solutions rapidly equilibrated with respect to pyrite, resulting in low $S^{-II}_{(aq)}$ concentrations. Rates of reductive pyrite dissolution were determined at 12 h from total $S^{-II}_{(aq+gas)}$ concentration vs. time data and were found to increase with temperature and H_2-partial pressure. The rate dependency on pH at 90 °C, 7 bar P_{H2} was regressed either with an asymmetric 'V'-shaped (two rate-pH domains) or a 'U'-shaped (three rate-pH domains) relation. For this reason, two separate kinetic rate laws were derived, based on the 'U'-regression (E_a = 35.2 kJ mol^{-1}):

$$r = 10^{-5.42} e^{-35208/RT} (P_{H_2})^{0.37} \left(1 - \frac{Q}{K_{eq}}\right)$$

or the 'V'-regression (E_a = 29.4 kJ mol^{-1}):

$$r = 10^{-5.13} e^{-29370/RT} (a_{H^+})^{0.13} (P_{H_2})^{0.37} \left(1 - \frac{Q}{K_{eq}}\right)$$

The performance of both rate laws was validated by reproducing the experimental $S^{-II}_{(aq)}$ concentrations in kinetic models. This comparison determined their applicability to be valid from 60 to 120 °C, 0-150 bar P_{H2}, and pH ~ 6.7-8.6 ('U' rate law) or pH ~ 4.1-8.6 ('V' rate law). The rate laws are compatible with geochemical reactive transport codes and will enhance the understanding of geochemical fluid-rock-gas interactions in H_2-bearing subsurface environments.

1. Introduction

Pyrite is the most abundant sulfide mineral in Earth surface environments (Rickard and Luther, 2007). While the oxidative dissolution kinetics of pyrite (FeS_2) by aqueous O_2 and Fe^{3+}-ions has been studied extensively in the scope of acid mine drainage (e.g., Nordstrom, 1982; Williamson and Rimstidt, 1994; Evangelou and Zhang, 2009; Holmes and Crundwell, 2000; Chandra and Gerson, 2010; Feng et al., 2019; Li et al., 2023), few experimental studies have been devoted to the reductive dissolution kinetics by dihydrogen (H_2) at shallow subsurface

* Corresponding authors.
E-mail addresses: robin.hintzen@univ-grenoble-alpes.fr (R. Hintzen), roland.hellmann@univ-grenoble-alpes.fr (R. Hellmann), vladimir.roddatis@gfz.de (V. Roddatis), Julia.vanWinden@shell.com (J. van Winden), laurent.truche@univ-grenoble-alpes.fr (L. Truche).

https://doi.org/10.1016/j.gca.2025.12.034
Received 14 July 2025; Accepted 16 December 2025
Available online 20 December 2025

temperatures (Truche et al., 2010, 2013).

Pyrite is a common but typically low abundance mineral constituent in clastic formations (~ < 0.1-2.0 wt%). The reductive dissolution of pyrite may therefore occur in the reservoir and caprocks of H_2-bearing engineered subsurface sites. Pyrite is prevalent in clay-rich host rocks used for nuclear waste disposal (Truche et al., 2010, 2013; Hendrix et al., 2022), where H_2 forms by the aqueous corrosion of steel cannisters enclosing radioactive waste (Gallé, 2000; Ortiz et al., 2002). In geologic reservoirs dedicated to carbon capture and storage, H_2 is introduced as a contaminant with the CO_2 injection stream from pre-combustion industrial sources (Thambimuthu et al. 2005; Oosterkamp and Ramsen, 2008). Pyrite occurs in sandstones of depleted natural gas fields and saline aquifers that are anticipated for the seasonal injection of H_2 as a means of large-scale subsurface energy storage (e.g., Bourgeois et al., 1979; Truche et al., 2013; Reitenbach et al., 2015; Hassannayebi et al., 2019; Labus and Tarkowski, 2022; Braid et al., 2024).

The reduction of minor amounts of pyrite in the presence of H_2 releases Fe^{+II} and important amounts of aqueous and gaseous sulfide species, i.e., $S^{-II} = H_2S_{(aq+gas)} + HS^-_{(aq)} + S^{2-}_{(aq)}$, given in Eqs. (1) and (2) (Truche et al., 2010, 2013; Hassannayebi et al., 2019). Depending on the acidity of the formation water, S^{-II} degasses to various extents from the aqueous fluid into the gas phase in the form of $H_2S_{(gas)}$ (Truche et al., 2010, 2013).

$$FeS_2 + H_2 = Fe^{2+} + 2HS^- \quad (1)$$

$$HS^-_{(aq)} + H^+ = H_2S_{(aq+gas)} \quad (2)$$

The released S^{-II} can trigger further reactions due to modifications of the redox potential, acidification and/or changing saturation states of minerals with respect to the pore water composition (Hassannayebi et al., 2019; Heinemann et al., 2021). At circumneutral to alkaline conditions (pH ~ 6.8-10), released S^{-II} is partly scavenged by pyrrhotite ($Fe_{1-x}S$) formation (Truche et al., 2013; Reitenbach et al., 2015; Hassannayebi et al., 2019). The following equation expresses the overall reaction (adapted from Hall (1986) and Truche et al. (2010) to meet the Fe-deficient non-stoichiometry of the pyrrhotite group; e.g., Lennie and Vaughan, 1996):

$$FeS_2 + H_2 = Fe_{1-x}S + H_2S_{(aq+gas)} + xFe^{2+} \quad \text{where } 0 < x < 0.125 \quad (3)$$

In the context of underground H_2 storage (UHS), where the injected H_2 gas is an economic asset, the geochemical reduction of pyrite by H_2 poses multiple potential challenges (Reitenbach et al., 2015; Heinemann et al., 2021; Zivar et al., 2021): *i)* economic loss of H_2 by reactive consumption, *ii)* contamination of the stored H_2 by $H_2S_{(gas)}$ formation, *iii)* changes in the reservoir porosity and permeability due to mineral dissolution/precipitation, *iv)* sulfide stress cracking and corrosion of the well infrastructure, and *v)* the need for potential surface facilities for $H_2S_{(gas)}$ removal from the extraction stream to allay health and safety concerns. A quantitative understanding of the rate of pyrite reduction is therefore crucial, but is hampered by a lack of sufficient experimental data at typical UHS conditions (Hassannayebi et al., 2019; Heinemann et al., 2021).

The reduction kinetics of pyrite has been studied by Truche et al. (2010, 2013) in the context of nuclear waste disposal. Truche et al. (2010) developed a kinetic rate law for S^{-II} production based on powder batch experiments at 90-180 °C and H_2 partial pressures (P_{H2}) of 8-18 bar. The reported form of their rate law is, however, not directly compatible with geochemical and reactive transport codes due to an intrinsic dependence on t^n (where t is time and n is the time exponent). Truche et al. (2013) performed additional experiments at 90 °C, 6 bar P_{H2} and at 150-250 °C from 0-30 bar P_{H2} using a pyrite-bearing claystone. In addition, the impact of the solution pH was assessed by equilibrium modeling (Truche et al., 2013), except for two experiments at pH 5 and pH 10 at 150 °C, 8 bar P_{H2} (Truche et al., 2010). These studies have provided valuable insights to the pyrite-pyrrhotite-H_2 system, but the dependence of the dissolution rate of pyrite at anticipated conditions for UHS (~ 30-140 °C, up to ~ 300 bar P_{H2}) is insufficiently covered.

The present study aims at determining reductive dissolution rates of pyrite at lower temperatures and high H_2 partial pressures in order to satisfy the critical need for kinetic data at UHS conditions. We conducted powder dissolution experiments of pyrite in aqueous H_2-pressurized solutions at conditions from 60-150 °C (7 bar P_{H2}), from 0-150 bar P_{H2} (90 °C) and $pH_{in\ situ}$ ~ 4-10 (90 °C, 7 bar P_{H2}). New kinetic rate laws for pyrite reduction are derived, with the developed equations being compatible with geochemical reactive transport codes. The present study thus enables future H_2 reservoir models to include abiotic sulfide formation rates based on experimentally derived kinetic rate laws for reductive pyrite dissolution.

2. Methods and materials

2.1. Solid reactants (pyrite and calcite)

The pyrite powder was obtained from a natural specimen (Huanzala mine, Peru) that was composed of several 2-6 cm large intergrown euhedral crystals. The sample was subjected to high voltage pulsed power selective fragmentation using the commercial Selfrag^{TM} system. Further grinding was performed in a mortar at ambient conditions. The 50-100 μm grain size fraction was recovered by sieving and cleaned for the removal of ultrafine surface particles based on the following procedure: *i)* 10-minute immersion (1x) in a static 0.5 M HCl solution, *ii)* 1-minute ultrasonification (2x) in 0.5 M HCl, *iii)* 1-minute ultrasonification (10x) in ultrapure water (UPW, 18.2 MΩ·cm), and *iv)* 1-minute ultrasonification (1x) in ethanol. The supernatant was discarded after each run. The cleaned pyrite grains were transferred into an Ar glove box ($[O_2] < 2$ ppmv) for drying and storage.

Powder X-ray diffraction (XRD) of the 50-100 μm fraction indicated the presence of small amounts of quartz (0.5 wt%) and native sulfur, S_8 (0.7 wt%) (Suppl. S.1–1, S.2–1). Scanning electron microscopy (SEM) showed inclusion-free pyrite grain surfaces. A few individual grains were found that were partly overgrown by a microscopic phase containing Fe, S, and O (Suppl. S.1–2).

Native sulfur was removed from the pyrite powder to avoid interferences with the quantification of sulfide release from pyrite dissolution. The removal protocol included thermal treatment at high vacuum conditions followed by washing in toluene ($C_6H_5CH_3$). The melting point of native sulfur at ambient conditions is 112.8 °C (Mandeville, 2010). Batches of ~ 8 g of the 50-100 μm grain size fraction were placed in elongated glass vials and heated to 80 °C from the bottom for 18 h under a secondary vacuum (6.7×10^{-6} bar). This led to the sublimation of native sulfur and its redeposition along the cool upper walls of the phials (Suppl. S.2–1). The native sulfur remaining in the pyrite powder was removed by washing three times for 1 min in undiluted toluene (Merck®, 34866-1L-M), a known solvent for native sulfur (Jay et al., 2009), followed by rinsing in ethanol. The complete removal of native sulfur was verified experimentally by comparing the sulfide release kinetics at the same conditions with a native S-free pyrite powder with the same grain size obtained from a different specimen (Suppl. S.2–2). The specific surface area (SSA) of the cleaned and purified 50-100 μm grain size fraction was 0.28 ± 0.002 $m^2\ g^{-1}$, determined by the BET method using Kr as the adsorption gas.

Calcite powder obtained from a transparent, euhedral specimen of Islandic spar was used as a carbonate buffer. The spar was first crushed in a mortar, sieved to recover the 200-600 μm fraction, and then was washed in UPW and ethanol.

2.2. Experimental methods

2.2.1. Experimental setup & reactor design

Hydrothermal reactors manufactured by the Parr Instrument Company® were used in different experimental setups. All reactors were

equipped with valves that permitted periodic in situ sampling of the reaction fluid via a reactor dip tube and adjustment of the reactor pressure without interruption of the reaction process. The temperature was continuously regulated to ± 1 °C by an external collar-furnace. The reactor vessel and head were sealed by a double-fringed PTFE© gasket and bolt-closure of both parts. Depending on the P_{H2}, two reactor types were used at different facilities to avoid hazards related to H_2-embrittlement.

Experiments at $P_{H2} \leq 7$ bar (90 %-Ar/10 %-H_2 gas mixture; grade 5.0, Messer®) were conducted in reactors made of pure titanium (grade 3). The reactor walls were passivated by a blue Ti-oxide surface layer that formed after heating the pressure vessel to 250 °C in the presence of 0.5 M HNO_3 solution overnight. Titanium is chemically inert with respect to H_2S over a wide pH range and was thus the preferred reactor material choice to avoid internal reactor wall sulfidation (Rauscher et al., 1990; Bodunrin et al., 2020). The use of Ti-reactors was in part based on previous pyrite dissolution studies that also used Ti-reactors for experiments at 8 bar P_{H2} up to 180 °C (Truche et al., 2010) and at 6 bar P_{H2} up to 250 °C (Truche et al., 2013). In the present study, two similar Ti-reactors were used, with each having an internal volume of 300 mL and equipped with a 90-bar rupture disk. The reactors were continuously stirred (130-140 rpm) by an internal impeller driven by an external magnetic drive. For experiments at 7 bar P_{H2} and temperatures > 100 °C, one of the Ti-reactors was equipped with a tap water cooling circuit to avoid boiling at the sampling valve and to prevent vapor-phase reactions in the stirring shaft. All experiments at $P_{H2} \leq 7$ bar using the Ar-H_2 gas mixture were carried out at the ISTerre hydrothermal laboratory, Univ. Grenoble Alpes (France).

Experiments at $20 \leq P_{H2} \leq 150$ bar (100 %-H_2 gas phase; grade 5.0, Messer®) were conducted in a Parr 316L stainless-steel reactor. For these experiments, stainless steel was chosen because the integrity of the Ti-reactors could not be guaranteed due to the potential risk of H_2-embrittlement and hydride-induced reactor wall cracking (TiH_x, with $0 < x \leq 2$) (Titanium Metals Corporation, 1997; Zhu et al, 2022). Several measures were taken to minimize the impact of internal reactor wall sulfidation on the measured dissolved sulfide concentrations in the 316L reactor: *i)* commercial application (SilcoTek®) of an amorphous functionalized silica-like coating (*a*-SiO_x:CH_y, Dursan®) to the reactor vessel, head, and dip tube, *ii)* use of a borosilicate glass liner (Parr Instrument®, 762HC2), and *iii)* wrapping of the dip tube and the thermocouple with PTFE® tape. The 316L reactor had an internal volume of 450 mL and was equipped with a 200-bar rupture disk. Stirring was performed periodically by a magnetic stir bar made of PTFE® that was placed at the bottom of the glass liner and driven externally. All experiments involving pure H_2 were carried out in an ATEX environment at Institut Néel, CNRS, Grenoble (France).

2.2.2. Experimental protocol

Reductive dissolution experiments of pyrite were run at variable *T*, P_{H2}, and pH conditions (Table 1) in 0.03 M NaCl aqueous solutions. A mass of 5 g L^{-1} pyrite (ø = 50-100 μm) and 12 g L^{-1} calcite (ø = 200-600 μm) were used. The Ti-reactors were set up with an initial solution volume of 200 mL, while 250 mL were used in the stainless-steel reactor. The same water/$rock_{py+cal}$ ratio of 58.8 mL g^{-1} was thus used in both setups. Experiments were initiated by Ar-purges of the reactors by three successive pressurizations to 10 bar (316L reactor) or 30 bar 100 %-Ar (Ti-reactors) in order to remove gaseous O_2 from the reactor head space and to check for gas leakages. A second deoxygenation step consisted of Ar-sparging the solution for 30 min via the reactor dip tube. The Ar-atmosphere was replaced by the respective H_2-bearing gas phase in a third pressurization cycle. In the final step, the reactors were first heated to the desired temperature and the total pressure subsequently adjusted to the desired P_{H2}. The starting time of each experiment ($t = 0$) corresponded to when the desired experimental conditions (*T*, P_{H2}) were reached.

The reaction progress during each experiment was monitored by chemical analyses of the experimental solution with 7-9 sampling steps over experimental run times ranging from ~ 700-900 h. The sampling protocol is described in section 2.2.3. The total volume of extracted solution after the penultimate sampling step did not exceed 30 vol% of the initial volume (except PY14, PY17, and PY19 with 35-43 vol%). The working pressure was reset after each sampling step. To avoid O_2-contamination of the reactor fluid during readjustment of the gas pressure, the gas line was flushed with an Ar-(H_2) gas and/or vacuum evacuated. Prior to the termination of each experiment, the composition of the H_2-bearing gas phase was qualitatively checked for undesired components (e.g., N_2, O_2) using a Perkin Elmer® CLARUS 500 gas chromatograph (GC) equipped with a thermal conductivity detector (TCD).

Table 1
Experimental conditions. Experiments in Ti-reactors were conducted using a 90 %-Ar/10 %-H_2 gas mixture, while experiments in stainless-steel (316L) reactors were performed using a 100 %-H_2 gas phase. The experimental solution was composed of 0.03 M NaCl. Deviations from these conditions are listed in the column 'pH buffer'. The in situ pH range gives the maximum spread of corrected and modeled pH estimates (section 2.3). n.a. = not applicable.

Expt #	Reactor	*T* (°C)	P_{H2} (bar)	Pyrite (g)	Calcite (g)	Solution (mL)	pH buffer	In situ pH range
Temperature dependence:								
#PY14	Ti	60	7	1.012	2.401	200	Calcite	9.1-9.3
#PY12	Ti	90	7	1.003	2.402	200	Calcite	8.6-8.8
#PY17	Ti	90	7	1.010	2.400	200	Calcite*	8.4-8.8
#PY13	Ti	120	7	1.005	2.401	200	Calcite	7.4-8.3
#PY15	Ti	150	7	1.007	2.400	200	Calcite	6.6-7.7
H_2 partial pressure dependence:								
#PY18	316L	90	20	1.252	3.002	250	Calcite	8.0-8.8
#PY23	316L	90	50	1.251	3.002	250	Calcite	7.8-8.7
#PY25	316L	90	100	1.252	3.004	250	Calcite	7.7-8.8
#PY27	316L	90	150	1.254	3.004	250	Calcite	7.6-8.8
pH dependence:								
#PY22	Ti	90	7	1.005	n.a.	200	8 bar P_{CO2}	3.8-4.2
#PY20	Ti	90	7	1.010	2.400	200	Calcite + 4 bar P_{CO2}	5.6-6.3
#PY19	Ti	90	7	1.004	2.400	200	Calcite + CO_3^{2-}/HCO_3^- **	9.0-10.1
#PY16	Ti	90	7	1.006	n.a.	200	$CaCO_3$ powder ***	9.0-10.5
Reference Ar-blank experiment:								
#PY21	Ti	90	0 (Ar)	1.004	2.401	200	Calcite	6.6-7.5

* Calcite grain size fraction of 50-100 μm.
** 30 mM CO_3^{2-}/HCO_3^- buffer (0.2003 g Na_2CO_3 + 0.3460 g $NaHCO_3$ in 200 ml of 30 mM NaCl).
*** $CaCO_3$ powder (AnalytiChem®, CL00.0302.2500), 2.400 g.

2.2.3. Sampling protocol & aqueous analysis

At each sampling step a specific sampling protocol for aqueous analysis was followed, based on the consecutive extraction of six solution aliquots from the reactor. The first aliquot (~ 2 mL) served to purge the sampling line and was discarded. The second aliquot (~ 1.5 mL) was first filtered (0.2 μm, cellulose acetate filter), then 1 mL of the filtered solution was acidified with 3 mL of 1 %-HNO_3 and stored at 4 °C. This aliquot was analyzed by inductively coupled plasma optical emission spectroscopy (ICP-OES, Varian® 720ES) to determine the elemental concentrations of dissolved B, Al, Si, Ca, and Fe. The third aliquot (~ 1 mL) was used for a pH measurement at ambient temperature (~ 25 °C). The three subsequent aliquots served to track the reductive dissolution of pyrite by quantification of the dissolved sulfide concentration ($S^{-II}_{(aq)} = H_2S_{(aq)} + HS^- + S^{2-}$), that is susceptible to devolatilization and oxidation. Three different analytical techniques were therefore used, namely Ag^+/S^{2-} ion-selective potentiometry, methylene blue spectrophotometry, and ICP-OES after H_2O_2-oxidation. Different aliquot pre-treatments adapted to each method were applied to maximize the sensitivity for the total sulfide in solution and for sulfide preservation. The techniques also vary in terms of applicable concentration ranges and potential interferences (e.g., Hoffmann, 1977; Millero et al., 1989; Fishman and Friedman, 1989; Lawrence et al., 2000; Baird et al., 2017). This multi-methodical approach ensured the accuracy of the $S^{-II}_{(aq)}$ determinations over a wide range of concentrations and evolving aqueous conditions with the reaction progress.

The fourth aliquot (~ 2 mL) was extracted directly from the sampling valve into a beaker prefilled with 2 mL of a strongly alkaline sulfide antioxidant buffer solution (SAOB: 2 M NaOH + $C_6H_8O_6$ + EDTA). At alkaline conditions the sulfide speciation shifts to $HS^-_{(aq)}$ and $S^{2-}_{(aq)}$, thus preventing the loss of H_2S by devolatilization. The dissolved sulfide concentration was then measured within < 10 min by potentiometry using the 'perfectION™ combination Ag^+/S^{2-}' ion-selective electrode (Mettler Toledo, 2011). Standardization of the electrode was performed using in-house standards, based on a newly purchased $Na_2S{\cdot}9H_2O$ salt (Thermo Scientific®, ref. 036622.30) that was continuously stored in an Ar-atmosphere glove box ($[O_2]$ < 2 ppmv). The concentrations of the standards were determined by the methylene blue method. The repeatability precision of the potentiometric protocol was ± 6.7 % (at 0.50 mM $S^{-II}_{(aq)}$, $n = 5$) based on the relative standard deviation (RSD%) of experimental aliquots.

The fifth aliquot (~ 0.1-3.9 mL) was extracted directly from the sampling valve into a sampling tube prefilled with 0.1 M $Zn(CH_3CO_2)_2$ in order to preserve the $S^{-II}_{(aq)}$ concentration as a ZnS suspension, followed by analysis using methylene blue spectrophotometry (Cline, 1969; Reese et al., 2011). The aliquot volume varied between ~ 0.1-3.9 mL depending on the previous potentiometric $S^{-II}_{(aq)}$ concentration estimate due to the requirement imposed by the Beer-Lambert law for analyte concentrations < 0.03 mM $S^{-II}_{(aq)}$. After addition of a mixed diamine reagent ([diamine] : $[Fe^{3+}]$ = 8.3 mM : 15.4 mM) to the stabilized and diluted aliquot, the methylene blue complex formed over a reaction time of 30 min. The samples were subsequently stored in the dark at 4 °C and their absorbances at 670 nm were measured within the same week of sampling using an Agilent® Cary 3500 UV-VIS spectrophotometer. Standardization of the spectrophotometer was based on the serial dilution of a $Na_2S{\cdot}9H_2O$ stock solution that was stabilized by $ZnCl_2$, stored in an Ar-atmosphere glove box, and whose sulfide concentration was determined by iodine back-titration (Baird et al., 2017). The repeatability precision of the methylene blue protocol was ± 9.7 % (at 0.01 mM $S^{-II}_{(aq)}$, $n = 4$), ± 6.3 % (at 0.05 mM, $n = 5$), and ± 7.3 % (at ≥ 0.7 mM, $n = 4$) based on the RSD% of experimental aliquots.

The sixth aliquot (~ 0.8 mL) was extracted directly from the sampling valve into a sample tube prefilled with 0.2 mL of 0.1 M Zn $(CH_3CO_2)_2$ for SO^{2-}_4-conversion. The aliquot was first oxidized by the addition of 3 mL 10 %-H_2O_2, then after an elapsed reaction time of ~ 1-2 h filtered (0.2 μm, cellulose acetate filter) and stored at 4 °C. The $S^{-II}_{(aq)}$ concentrations in the oxidized aliquots were indirectly determined within a few months as total elemental sulfur by ICP-OES. The repeatability precision of the SO^{2-}_4-conversion protocol was ± 10.3 % (0.7 mM $S^{-II}_{(aq)}$, $n = 5$), based on the RSD% of experimental aliquots. Measurements by ICP-OES of an elemental sulfur control (IV-stock 29, Inorganic Ventures®), after dilution to 2.063 ppm (0.064 mM), yielded an accuracy of ± 5 %.

The sum of the total extracted sample volume at each sampling step ranged between 6.3-12.8 mL for all experiments.

2.2.4. Post-mortem analysis of solids

After cooling of the reactors (~ 45 min), the altered solids were washed in UPW and ethanol before being transferred to an Ar-atmosphere glove box for drying and storage. The altered solids were analyzed by X-ray diffraction (XRD) using a Bruker® D8Advance diffractometer with Cu Kα radiation (λ = 1.5406 Å, 40 kV, 40 mA). The acquisition time was 32 s at a 2Θ-step size of 0.026°. Mineral quantification was performed by Rietveld refinement, using the BGMN program with the Profex user interface (Doebelin and Kleeberg, 2015). A Zeiss® GeminiSEM 500 equipped with a Schottky-type field emission gun was used for the micrometer scale investigation of the altered pyrite grains. An ~ 1 nm-Au/Pd coating was applied before secondary electron (SE) imaging with a maximum resolution of 0.6 nm at 15 kV and 1.1 nm at 1 kV. Nanometer-scale analyses of reacted pyrite surfaces and authigenic secondary mineral phases was performed using a Thermo Fisher Scientific® Themis Z (3.1) scanning transmission electron microscope (STEM) operated at 300 kV. This TEM is equipped with aberrations corrector at the probe side, a SuperX® energy dispersive X-ray (EDX) spectrometer, and a Gatan Continuum 1065ER electron energy loss spectrometer (EELS). Ultrathin cross-sections of samples were prepared by the focused ion milling (FIB) lift-out method (Overwijk et al., 1993) using an FEI Helios G4 UC Ga-dual beam FIB-SEM.

2.3. Experimental calculations

The calculations described in the sections 2.3.1 and 2.3.2 were executed using the geochemical code PHREEQC (Parkhurst and Appelo, 2013) with the Thermoddem database (Blanc et al., 2012). Aqueous speciation reactions containing carbon species with a non-(+IV) valence state (e.g., CH_4, CO) were redox-decoupled by modification of the equilibrium constants in order to suppress the reduction of carbonate species (e.g., HCO_3^-) into CH_4 by H_2. These reactions are kinetically inhibited within the time scale and conditions of the experiments (Seewald et al., 2006; Vialle and Wolff-Boenisch, 2024), which was confirmed by the absence of CO and CH_4 in the gas phase of the experiments.

The measured solution pH at laboratory bench conditions deviates from the pH in the reactor at experimental conditions, and therefore requires modification. Two estimates of the in situ pH were calculated, one based on correction of the measured pH at ambient conditions ('corrected $pH_{in\ situ}$', section 2.3.1), and the other based on pyrite titration modeling ('modeled $pH_{in\ situ}$', section 2.3.2).

2.3.1. Correction of measured pH

Extrapolation of the measured pH value from ambient to experimental conditions was performed by re-equilibration of the solution composition with respect to the experimental *T*, total *P*, and partial pressures of gases (H_2, Ar, CO_2). The input for the solution composition included the measured pH, the initial NaCl matrix, the $S^{-II}_{(aq)}$ concentration from methylene blue spectrophotometry, and the major element concentrations from ICP-OES. In addition, a total dissolved carbonate concentration equal to the measured concentration of dissolved Ca was assumed, based on the stoichiometric dissolution of calcite (e.g., Pokrovsky et al., 2005). Degassing of CO_2 was neglected in the models because in situ CO_2 formation was not detected by GC.

2.3.2. Pyrite titration models

All experiments were simulated as pyrite titration models (PTM) in order to derive complementary kinetic parameters. These models thermodynamically reproduce the kinetically-driven reductive dissolution of pyrite by the stepwise dissolution of defined moles of pyrite. For a given experiment the input to the model uses the cumulative number of moles of dissolved pyrite at each sampling step. This quantity corresponds to the total amount of sulfide released into the reactor, which is partitioned into the following sinks: *i)* aqueous sulfide, *ii)* gas phase sulfide, and *iii)* sulfide incorporated into secondary minerals. The quantitative estimation of sulfide in these sinks at each sampling step is provided in the supplementary materials (section S.3). Section S.3 also contains details on the workflow and input file scripts of the PTMs. These models provided a complete and thermodynamically consistent quantification of the fluid-mineral-gas equilibrium at each sampling step in all experiments, from which, for example, the modeled $pH_{in\ situ}$, $H_2S_{(gas)}$, and saturation index of pyrite (SI_{FeS2}) were retrieved. The PTMs were validated by comparing the Ca concentrations that were modeled versus those measured by ICP-OES (Suppl. S.5). An average absolute deviation of 11 % was determined with respect to the calcite-buffered experiments.

2.3.3. Dissolution rates

The dissolution rates of pyrite reported in this study were determined from instantaneous changes in the sulfide concentration with time. As opposed to flow-through reactor systems, the concentrations of reaction products continuously change with time in batch reactor systems. For this reason, an infinite number of rates can be determined from experimental concentration vs. time data in the latter. In this study, the dissolution rates were consistently determined at 12 h. Albeit subjective, this choice was a compromise between earlier rates (< 12 h), where rapid dissolution of remaining surface fines may result in artificially elevated sulfide release rates, and later rates (> 12 h), characterized by an increasing impact of secondary mineral precipitation on the measured kinetics. As further discussed in section 4.3, in batch reactor systems initial rates are most representative of plateau rates, which is synonymous with far-from-equilibrium conditions of dissolution (e.g., Nagy and Lasaga, 1992; Oelkers, 2001; Beig and Lüttge, 2006; Hellmann et al., 2006).

The rates at 12 h were determined from concentration vs time data that was composed of the aqueous sulfide concentration and the moles of gaseous sulfide. For the dissolved sulfide, the measured concentrations by methylene blue spectrophotometry ($C^{MB}_{S^{-II}_{(aq)}}$, [M]) were used, as this was the only technique with a sufficiently low detection limit to consistently cover all experiments. Because the available GC-TCD technique did not allow for the direct measurement of degassed sulfide, we instead estimated $H_2S_{(gas)}$ [mol] from the PTMs (section 2.3.2). However, the fraction of $H_2S_{(gas)}$ to $H_2S_{(aq+gas)}$ at the initial time steps was only significant (> 5 %) in experiments run at acidic pH conditions (PY20, PY22). In all other experiments, the estimated $H_2S_{(gas)}$ fractions from the PTMs to the total sulfide released from pyrite were negligible at 12 h, but were nonetheless considered. The aqueous and gaseous sulfide data were converted into moles of dissolved pyrite per surface area (n_{FeS_2}, [mol m^{-2}]) at each sampling step *i*:

$$n_{FeS_2} = \frac{\left[\left(C^{MB}_{S^{-II}_{(aq)}} \times V_{sol}\right) + H_2S_{(gas)}\right]_i}{mass_{py} \times SSA \times k = 2} \tag{4}$$

where V_{sol} [L], $mass_{py}$ [g], and SSA [$m^2\ g^{-1}$] are the solution volume prior to aliquot extraction, the starting mass of pyrite powder, and the specific surface area, respectively. All rate calculations used a constant *SSA* that was determined before the experiments (section 2.1). Post-alteration *SSA* values were not measured due to: *i)* insufficient pyrite sample mass for BET analysis, *ii)* mixing of pyrite and calcite grains, *iii)* the determination of initial dissolution rates for which post-mortem surface areas are not accurate, and *iv)* contribution of secondary mineral surface areas to post-reaction pyrite surface areas.

The data sets of n_{FeS_2} as a function of time for each experiment were fit with the Michaelis-Menten (M-M) equation, given in Eq. (5), whose use does not imply any underlying reaction mechanism. The first derivative of the M-M equation, given in Eq. (6), allowed for the instantaneous rate to be determined at any time, i.e., at 12 h in the present study.

$$f(x) = \frac{mx}{n+x} \tag{5}$$

$$\frac{df(x)}{dx} = \frac{m}{n+x} - \frac{mx}{(n+x)^2} \tag{6}$$

In both equations above, x is the time [s] and m and n are fitting parameters. In most experiments, the fits were restricted to the initial two to four data points. The graphs illustrating the M-M fits for each experiment are shown in the supplementary section S.5.

3. Results

3.1. Pyrite alteration and secondary mineral formation

Overall, the fraction of pyrite that was altered and dissolved by H_2 over the timescales of the experiments was small relative to the amount of pyrite available. Based on the estimations of total reacted pyrite (section 2.3.2, Suppl. S.3), in the most reactive experiments, PY15 (150 °C, 7 bar P_{H2}) and PY27 (90 °C, 150 bar P_{H2}), a total of only 6.9 mol% and 1.4 mol% of pyrite was dissolved, respectively. However, the different degrees of pyrite alteration and secondary mineral formation that occurred as a function of T, P_{H2}, and pH were striking. These differences are illustrated in the compilation of SEM images shown in Fig. 1.

The unaltered pyrite grains (Fig. 1 A) showed smooth surfaces and some microrelief with sharp edges. Some minor ultrafine surface particles remained after the cleaning procedure. Observation of the altered pyrite grains at 90 °C, 70 bar Ar, and in the absence of H_2 (Fig. 1 B), revealed no textural differences with respect to the unaltered pyrite. In the presence of low partial pressures of H_2, ultrafine surface particles appeared to have dissolved (e.g., Fig. 1 C) and secondary mineral phase formation started to occur. In general, the predominant reaction products in most experiments included octahedral crystals < 0.5 μm in diameter (Fig. 1 M) and up to μm-sized, pseudo-hexagonal crystals (Fig. 1 N). The elemental concentration distributions of S, Fe, and O (Fig. 2 B-D) showed that the former crystals are Fe-oxides, whereas the latter are Fe-sulfides. These phases were identified as magnetite (Fe_3O_4) and pyrrhotite ($Fe_{1-x}S$), respectively, using selected area electron diffraction (SAED) and high-resolution STEM imaging (Fig. 2). Based on the stoichiometric mole fractions of S, pyrite (66.7 mol% S) and pyrrhotite (50.0-53.3 mol% S, for $0 \leq x \leq 0.125$) were clearly distinguishable by element mapping (Fig. 2 C). The mole fractions of S demonstrate that not all of the S released from pyrite is incorporated into pyrrhotite.

At 7 bar P_{H2} and increasing temperatures from 60 °C to 150 °C (Fig. 1 C, D, E, G), the abundance and crystal growth of coexisting euhedral pyrrhotite and magnetite increased. At 60 °C and 90 °C, their abundances were limited, and magnetite dominated over pyrrhotite. At temperatures ≥ 120 °C, the formation and growth of pyrrhotite significantly increased while the abundance of magnetite decreased. At 150 °C, secondary pyrrhotite covered roughly half of the surface area of primary pyrite particles with an abundance of ~ 4 wt% based on quantification by powder XRD, while magnetite was below the detection limit. The quantification of secondary minerals by XRD at less reactive conditions (< 150 °C) was not possible due to their low mass fractions relative to pyrite. The observed secondary minerals in this study agree in

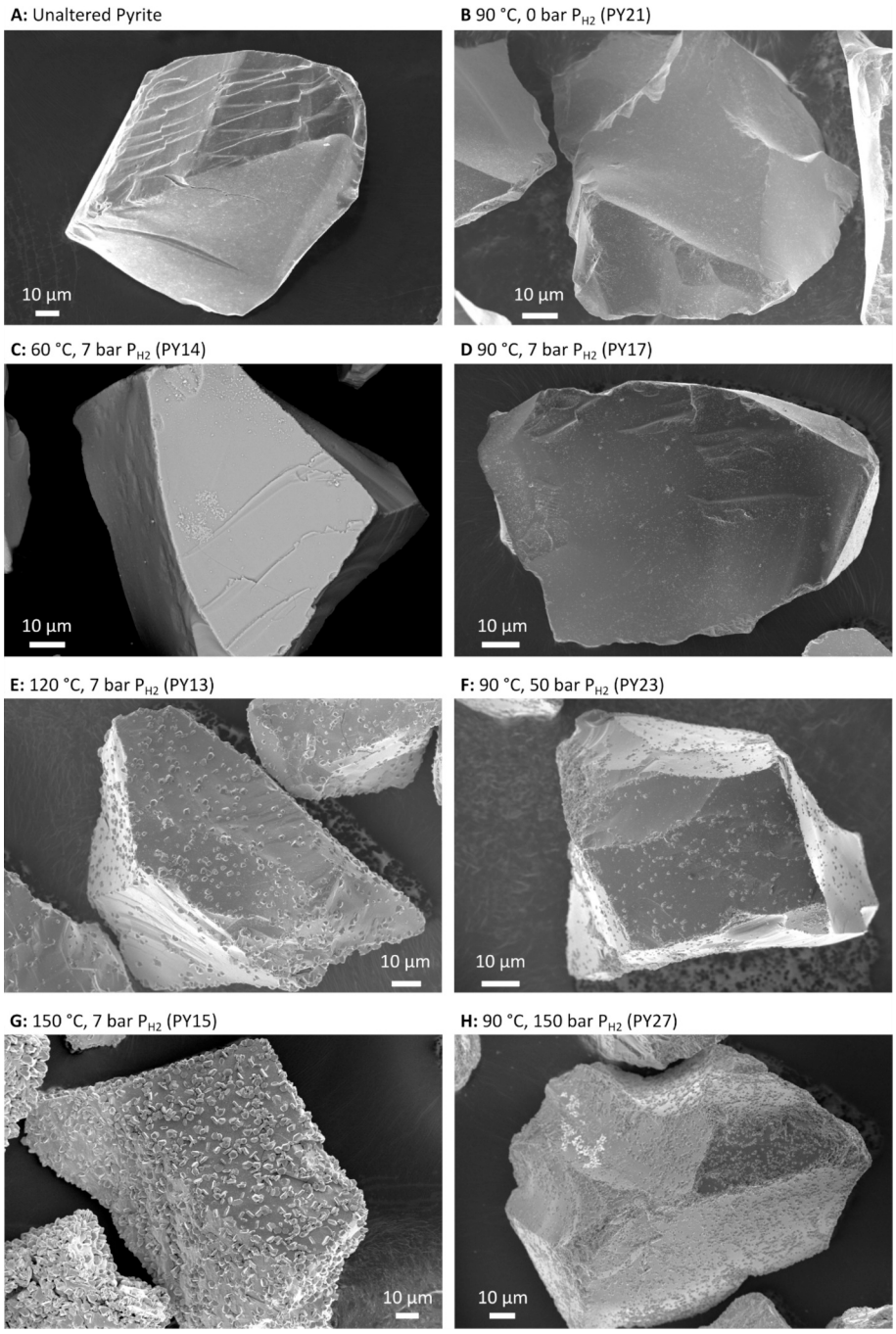

Fig. 1. Secondary electron SEM images of post-mortem pyrite grains from various experimental conditions after 700-900 h of alteration (except B: 405 h, E: 520 h, and K: 1054 h). The *T*-experiments from 60 to 150 °C at 7 bar P_{H2} (C, D, E, G) and the P_{H2}-experiments from 0-150 bar at 90 °C (B, D, F, H) were calcite-buffered. Grains from these experiments showed that increasing *T* and P_{H2} led to enhanced formation of pyrrhotite, with variable abundances of magnetite. The pH-experiments (D, I, J, K, L) used various buffering mechanisms (Table 1) at 90 °C and 7 bar P_{H2}. Given corrected pH values refer to experimental in situ conditions. Individual remarks: A: Unaltered pyrite grain after ultrasonic cleaning and purification for native sulfur removal. B: No secondary mineral formation in the absence of H_2. I: No visible secondary mineral formation at 8 bar P_{CO2}-buffered, acidic conditions. J: Growth of rhombohedral CaFe-carbonate (likely ankerite) along the edge of the pyrite grain in 4 bar P_{CO2}-buffered, slightly acidic conditions with calcite; pyrrhotite was sparse. K: Coexistence of abundant magnetite and pyrrhotite at CO_3^{2-}/HCO_3^--buffered, intermediate alkaline conditions. L: Formation of a ferric iron-bearing phase in coexistence with abundant magnetite at alkaline conditions. The clumps of aggregated grains on the sample mount are the commercial $CaCO_3$ powder used for pH-buffering; no pyrrhotite formation. M and N: Magnified images of magnetite and pyrrhotite formation from select experiments (PY17, PY15) on primary pyrite. The very small and bright dispersed grains in N are magnetite crystals.

part with those reported in Truche et al. (2010). In their experiments, only pyrrhotite was observed as a product of pyrite reduction. Even though thermodynamic modeling predicted the formation of magnetite during the early stages of reaction, this phase was never observed directly in their study.

With increasing partial pressure of H_2 from 0 bar to 150 bar at 90 °C (Fig. 1 B, D, F, H), the abundance of pyrrhotite increased steadily, but without a systematic impact on the crystal size. This is contrary to the

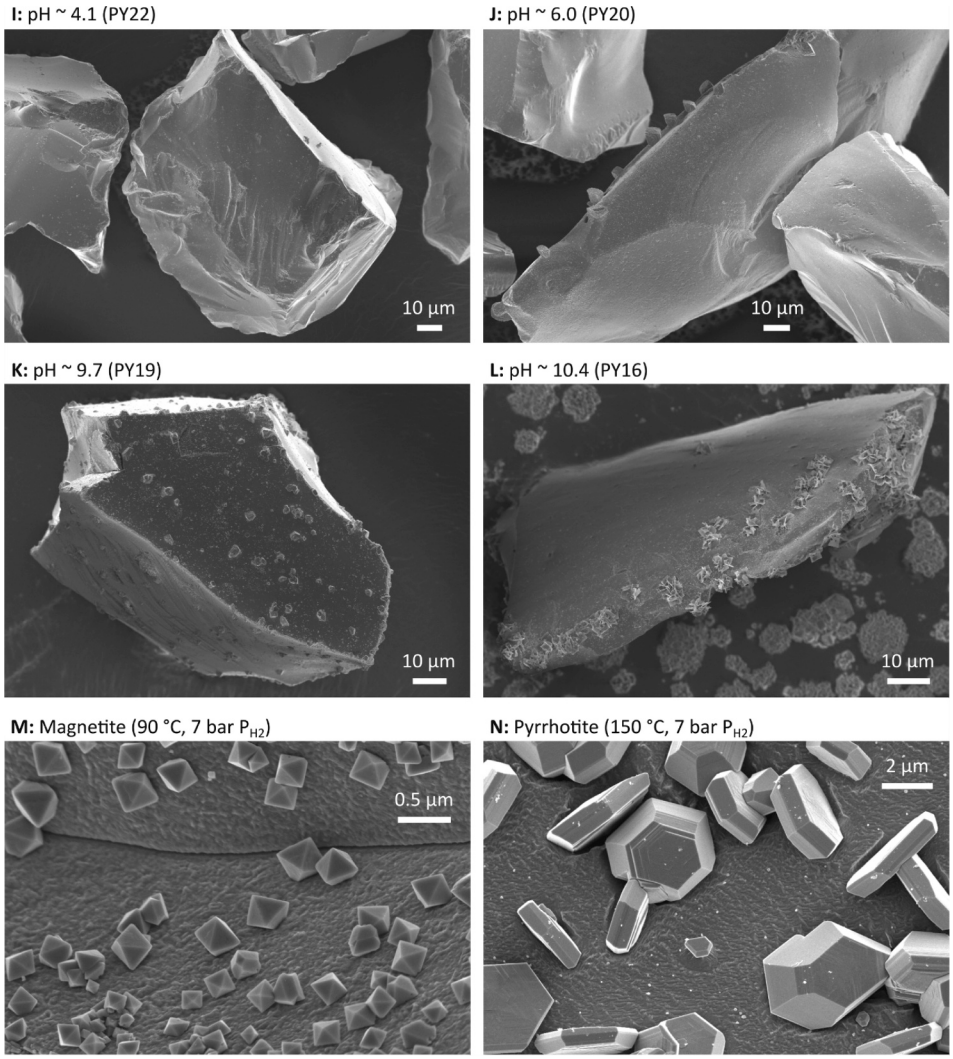

Fig. 1. (*continued*).

effect of temperature on pyrrhotite crystallization. Except for the experiment at 7 bar P_{H2}, no octahedral magnetite crystals were found after runs at elevated partial pressures of H_2.

The degree of pyrite alteration and secondary mineral formation at 90 °C and 7 bar P_{H2} were a strong function of pH. Our experimental observations confirm models from Truche et al. (2013) which predicted low reactivity at acidic pH and a sharp increase at the onset of alkaline conditions. In the present study at a corrected $pH_{in\ situ}$ ~ 4.1 (8 bar P_{CO2}-buffered; Fig. 1 I), the growth of secondary minerals was not observed and many ultrafine particles remained on the pyrite surface, even after 714 h of pyrite alteration. A few areas were found with evidence for limited dissolution of pyrite in the form of surface etch pits. In the presence of calcite at a corrected $pH_{in\ situ}$ ~ 6.0 (4 bar P_{CO2}-buffered; Fig. 1 J), µm-sized rhombohedral crystals of a CaFe-carbonate (likely ankerite) precipitated as the main secondary mineral. Here again, remaining ultrafine surface particles incompletely dissolved. Except for highly fractured sites, very few individual pseudo-hexagonal grains (i.e., pyrrhotite) with a size < 100 nm were observed. Nonetheless, these results show reactivity of pyrite with H_2 at acidic pH, albeit limited.

The alteration of pyrite significantly intensified with increasing pH at slightly alkaline conditions, as did the degree of secondary mineral formation. The experiment at a corrected $pH_{in\ situ}$ ~ 8.6 (calcite-buffered; Fig. 1 D, M) yielded the first evidence for coexisting magnetite and pyrrhotite. The abundance and crystal growth of both phases increased at a corrected $pH_{in\ situ}$ ~ 9.7 (CO_3^{2-}/HCO_3^--buffered; Fig. 1 K). In the experiment at a corrected $pH_{in\ situ}$ ~ 10.4 ($CaCO_3$ powder buffer; Fig. 1 L), µm-sized tabular crystals with a thickness < 50 nm formed, rather than pyrrhotite. These coexisted with abundant magnetite. Powder XRD and TEM data reveal that these crystals are either ferric oxy-hydroxides or ferric oxy-hydroxy-sulfates. Oxygen contamination was excluded by GC measurements upon termination of the experiment. Similar evidence for oxidation at alkaline conditions in a reducing H_2-rich environment was observed in a NaOH-buffered experiment (150 °C, 8 bar P_{H2}, pH ~ 10) by Truche et al. (2010). They observed a brown solution after 100 h, which they attributed to colloidal Fe-oxy-hydroxides. Such oxidative alteration at constant reducing redox potential is expected for highly alkaline solutions, based on thermodynamic phase equilibria (Rickard and Luther, 2007).

The SEM images in Fig. 1 were selected to show the variability of alteration intensity of pyrite reduction as a function of T, P_{H2}, and pH. In addition, significant differences in terms of reactivity were noted when examining multiple grains from the same experiment. Secondary growth of minerals was commonly more pronounced in areas of exposed microrelief, such as corners, edges, and fractured areas. Differences in secondary mineral abundance also occurred between adjacent surfaces of the same grain. This may indicate differential dissolution and growth with respect to crystallographic orientations, despite the apparent isotropy of pyrite (Lambert et al., 1998; Liu et al., 2021). Variable degrees of secondary mineral formation may also be related to hydrodynamic effects within the grain aggregate at the reactor bottom.

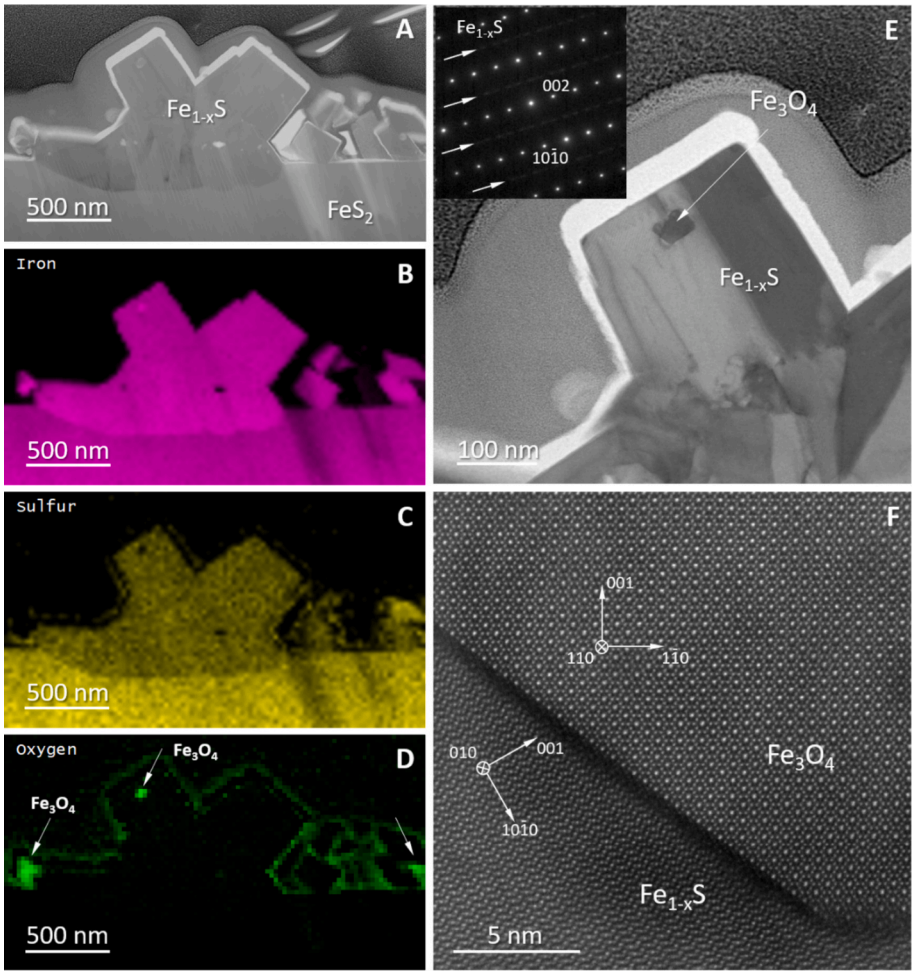

Fig. 2. Pyrrhotite ($Fe_{1-x}S$) and magnetite (Fe_3O_4) characterized by TEM techniques. A: High-angle annular dark-field (HAADF) image of secondary mineral formation on primary pyrite (FeS_2) altered at 90 °C and 7 bar P_{H2} (PY17). B, C, D: EELS maps of iron (L3,2-edge at ~ 708 eV), sulfur (K-edge at ~ 2 472 eV), and oxygen (K-edge at ~ 532 eV), respectively. E: Bright field (BF) image and SAED (inset) of pyrrhotite in [010] orientation. The white arrows in the SAED point out streaks originating from defects in the pyrrhotite crystal structure. F: A high-resolution STEM image of the interface between pyrrhotite and the magnetite inclusion (along [110]) displayed in E.

3.2. Sulfide formation and aqueous composition

The total aqueous and gaseous sulfide ($S^{-II} = H_2S + HS^- + S^{2-}$) measurements from all dissolution experiments of pyrite normalized to the surface areas varied from 10^{-6}-10^{-3} mol m^{-2}. Steady-state conditions were achieved within ~ 300-500 h for experiments characterized by final dissolved sulfide concentrations ≤ 0.12 mM (e.g., PY12, PY14, PY17, PY18, PY20). Experiments with higher dissolved sulfide concentrations did not achieve an unambiguous steady state within ~ 700-800 h. A summary of all aqueous data ($S^{-II}_{(aq)}$, pH, ICP-OES) for each experiment is given in the supplementary section S.5. The temporal evolution of sulfide formation as a function of T, P_{H2}, and pH is given in the following sections.

3.2.1. Temperature dependency

Sulfide concentrations from pyrite dissolution, encompassing both measured aqueous and calculated gaseous species, showed a positive but non-linear correlation with temperature. The release of sulfide to solution proceeded rapidly initially and tended to slow down with time (Figs. 3-5). The magnitude of sulfide concentrations was markedly different at temperatures ≤ 90 °C and ≥ 120 °C (Fig. 3). All of the temperature series experiments were calcite-buffered and performed at the same H_2 partial pressure (7 bar P_{H2}). At 60 °C and 90 °C, steady-state sulfide production of ~ 0.005 mmol m^{-2} (0.01 mM $S^{-II}_{(aq)}$) and ~ 0.025 mmol m^{-2} (0.05 mM $S^{-II}_{(aq)}$) were achieved over the experimental durations. The fraction of gaseous H_2S was ≤ 2.2 mol% of the total aqueous and gaseous sulfide for both experiments, with the corrected $pH_{in\ situ}$ remaining nearly constant (pH 9.1-9.3 at 60 °C, pH 8.4-8.7 at 90 °C) (Suppl. S.5-3, S.5-6). At higher temperatures, total sulfide formation increased significantly to ~ 0.35 mmol m^{-2} (0.63 mM $S^{-II}_{(aq)}$) after 520 h at 120 °C and 2.0 mmol m^{-2} (2.7 mM $S^{-II}_{(aq)}$) after 744 h at 150 °C (Fig. 3). At the end of these experiments, the fractions of $H_2S_{(gas)}$ relative to the total aqueous and gaseous sulfide were 11.4 mol% and 33.0 mol%, respectively. The differences in sulfide concentrations as a function of temperature correlate with the different degrees of secondary pyrrhotite formation (section 3.1).

After the initial onset of rapid sulfide formation, both high temperature experiments (120 °C, 150 °C) were characterized by a short period of slower kinetics between ~ 30-80 h, which was then followed by accelerated sulfide release. These non-monotonic changes in the kinetics were captured in both experiments by all sulfide analytical methods (Fig. S.5-2a, Fig. S.5-4a).

In the 120 °C and 150 °C experiments, the fraction of gaseous H_2S continuously increased over the course of the experiments, while the modeled in situ solution pH decreased from pH 8.2 to 7.4 at 120 °C (Suppl. S.5-2) and from pH 7.7 to 6.7 at 150 °C (Suppl. S.5-4). The measured Ca concentrations correlated positively with increasing temperature, decreasing pH, and total sulfide formation. At 60 °C and 90 °C,

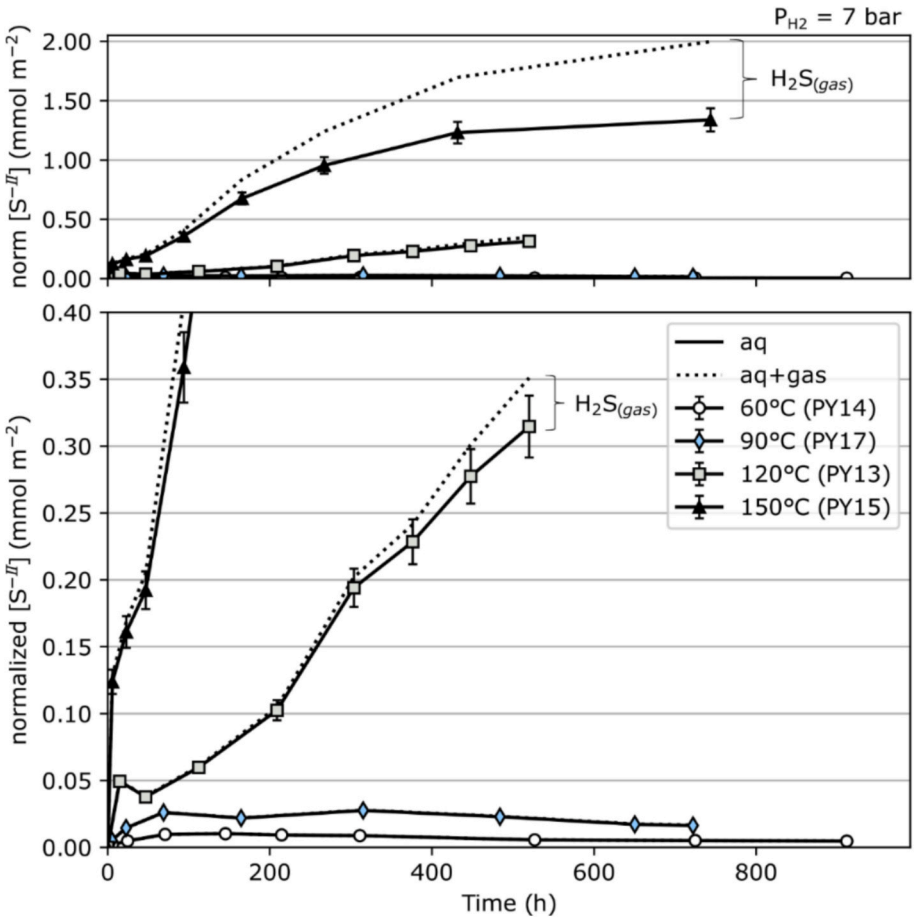

Fig. 3. Temporal evolution of aqueous and gaseous moles of sulfide normalized to the surface areas of pyrite as a function of temperature from 60-150 °C ($P_{H2} = 7$ bar). Aqueous sulfide concentrations were measured by methylene blue spectrophotometry. Gaseous H_2S concentrations were determined from thermodynamic equilibria in pyrite titration models. Panel B is a close-up of panel A.

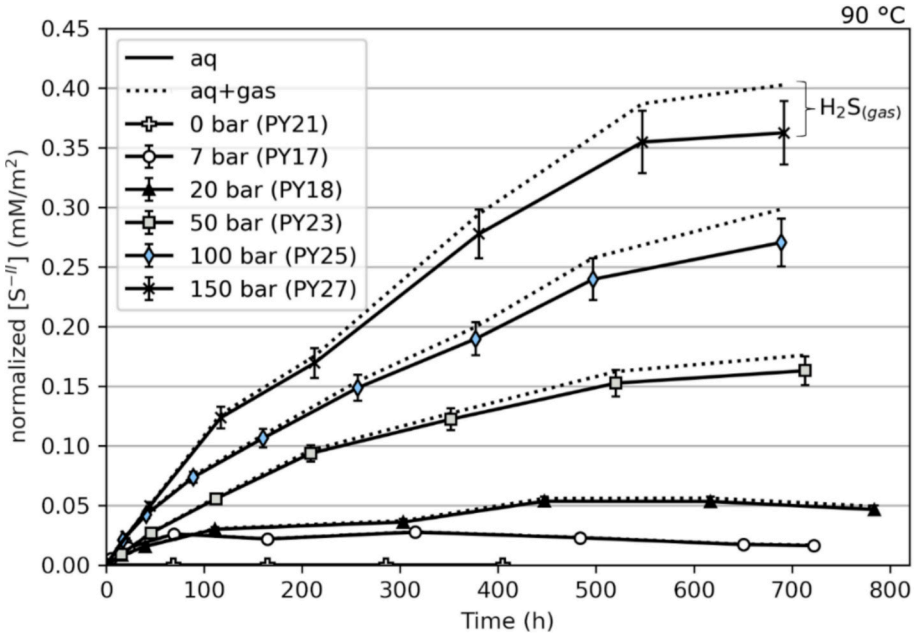

Fig. 4. Temporal evolution of aqueous and gaseous moles of sulfide normalized to the surface area of pyrite as a function of the partial pressure of H_2 from 0-150 bar (90 °C). Aqueous sulfide concentrations were measured by methylene blue spectrophotometry. Gaseous H_2S concentrations were determined from thermodynamic equilibria in pyrite titration models.

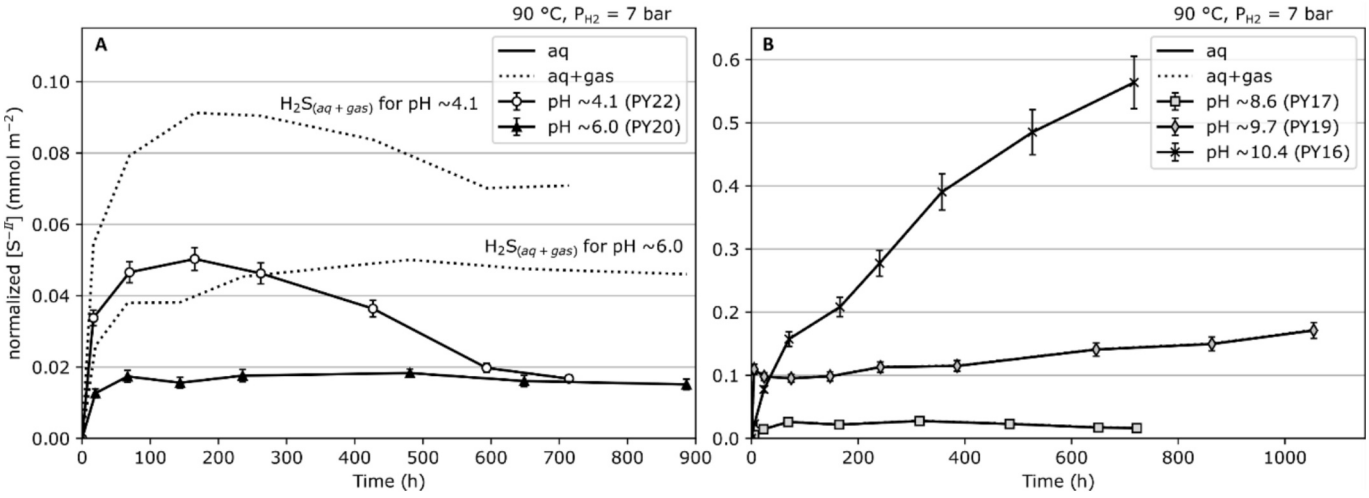

Fig. 5. Temporal evolution of aqueous and gaseous moles of sulfide normalized to the surface areas of pyrite at acidic (A) and alkaline (B) conditions (90 °C, $P_{H2} = 7$ bar). Aqueous sulfide concentrations were measured by methylene blue spectrophotometry. Gaseous H_2S concentrations were determined from thermodynamic equilibria in pyrite titration models. The mole fractions of $[H_2S]_{(gas)}$ relative to total aqueous and gaseous sulfide were insignificant at alkaline conditions (B).

near-constant concentrations between 0.2-0.3 mM Ca were measured (Suppl. S.5-3, S.5-6), while at 120 °C and 150 °C these increased to final values of 0.48 mM and 1.30 mM Ca, respectively (Suppl. S.5-2, S.5-4). Aqueous Fe was not detected in any temperature series experiment based on ICP-OES measurements.

3.2.2. *H_2 partial pressure dependency*

In the experiments of variable H_2 partial pressure, sulfide release from pyrite reduction increased from 7 bar to 150 bar P_{H2} at a constant temperature of 90 °C (Fig. 4). Steady-state normalized total aqueous and gaseous sulfide formation of ~ 0.025 mmol m^{-2} (0.05 mM $S^{-II}_{(aq)}$) and ~ 0.050 mmol m^{-2} (0.11 mM $S^{-II}_{(aq)}$) were obtained at 7 bar and 20 bar P_{H2}, respectively. The fraction of $H_2S_{(gas)}$ accounted for ≤ 5.6 mol% in both experiments. Near steady-state sulfide release increased from ~ 0.18 mmol m^{-2} (0.36 mM $S^{-II}_{(aq)}$) at 50 bar P_{H2} to ~ 0.40 mmol m^{-2} (0.77 mM $S^{-II}_{(aq)}$) at 150 bar P_{H2} after ~ 700 h of reaction time. In the latter experiment, 10.0 mol% of the total aqueous and gaseous sulfide was in the gas phase. In the absence of H_2 (PY21), no detectable aqueous sulfide was measured by methylene blue spectrophotometry and potentiometry. This clearly indicates that the reactivity of pyrite at anoxic conditions requires the presence of H_2 as the reductant.

In the experiments at 20-150 bar P_{H2}, also elevated concentrations of dissolved Si (10^{-3} M) and B (10^{-4} M) were measured, likely due to leaching of the borosilicate glass liner used in the 316L stainless-steel experiments (Suppl. S.5-7, S.5-12, S.5-13, S.5-14). The modified solution composition affected the measured solution pH at 25 °C, as it was shifted to initially slightly more alkaline conditions (pH ~ 8.7-9.2) relative to the 90 °C experiments in Ti-reactors without glass liners. However, the initial values of the corrected $pH_{in\ situ}$ at experimental temperature were in the same range (pH ~ 8.6-8.8). The modeled $pH_{in\ situ}$ in equilibrium with calcite from the PTMs predicted an acidification trend of the solutions in all experiments from 20-150 bar P_{H2}, which correlates with increased sulfide formation. This trend was mimicked by increasing Ca concentrations with time. To illustrate this at 150 bar P_{H2} (e.g., Suppl. S.5-14), the modeled $pH_{in\ situ}$ decreased from pH 8.5 to pH 7.6, while simultaneously $S^{-II}_{(aq)}$ and Ca concentrations increased to 0.77 mM and 0.78 mM, respectively. As in the *T*-series, aqueous Fe was also not detected in the P_{H2} experiments based on ICP-OES measurements.

3.2.3. *pH dependency*

The normalized total aqueous and gaseous sulfide formation for pyrite dissolution experiments conducted at different pH is shown in Fig. 5. As expected, sulfide formation at constant temperature (90 °C) and H_2 partial pressure (7 bar P_{H2}) increased from neutral to alkaline pH conditions (Fig. 5 B). Surprisingly, sulfide formation also increased from neutral to acidic conditions, albeit by a much lower degree (Fig. 5 A). In addition, the proportion of gaseous sulfide was high at acidic conditions, whereas at alkaline conditions the released sulfide was nearly all aqueous. As a reminder, neutral pH in pure H_2O at 90 °C and 70 bar is pH ~ 6.2 (calculated after IAPWS, 2019).

In the CO_2-buffered experiments, the normalized total aqueous and gaseous sulfide release yielded peak concentrations of ~ 0.05 mmol m^{-2} (0.03 mM $S^{-II}_{(aq)}$) at a corrected $pH_{in\ situ}$ ~ 6.0, and increased further to ~ 0.09 mmol m^{-2} (0.08 mM $S^{-II}_{(aq)}$) at $pH_{in\ situ}$ ~ 4.1 (Fig. 5 A). After the peak concentration was reached at 165 h in the pH 4.1 experiment, the dissolved sulfide concentrations decreased to 0.03 mM $S^{-II}_{(aq)}$, indicating sulfide redistribution into other species and phases. The fraction of $H_2S_{(gas)}$ increased with time in both experiments and attained 76.4 mol % (PY22) and 67.1 mol% (PY20) of total aqueous and gaseous sulfide. The experiments at acidic conditions were the only ones where a significant Fe concentration was measured in solution, with 0.6-0.7 mM Fe at pH ~ 4.1 (Suppl. S.5-11) and decreasing concentrations of Fe from 0.35 mM to 0.14 mM at pH ~ 6.0 (Suppl. S.5-9). The modeled $pH_{in\ situ}$ remained nearly constant in both experiments.

Sulfide release during pyrite dissolution at elevated alkaline conditions (corrected $pH_{in\ situ} \geq 9.7$) exceeded the sulfide formation at acidic conditions by an order of magnitude, despite the same *T* and P_{H2} conditions (Fig. 5). In these experiments (PY19, PY16), the measured aqueous sulfide concentrations continuously increased over the duration of the experiments (Fig. 5 B). The fraction of $H_2S_{(gas)}$ remained ≤ 0.4 mol %. Only in the lower alkaline experiment at pH ~ 8.6, did the steady-state dissolved sulfide formation (~ 0.025 mmol m^{-2}, 0.05 mM $S^{-II}_{(aq)}$) resemble the concentration levels of the acidic experiments.

Difficulties were encountered in the PTMs of the experiments at elevated alkaline conditions (PY19, PY16) because the reactivities of the chemical products used as pH buffers ($CaCO_3$, Na_2CO_3, $NaHCO_3$) were too different compared to the corresponding mineral phases of the same composition included in the database. This explains some of the deviations in the measured and modeled parameters (see remarks in Suppl. S.5-5, S.5-8).

3.3. *Reductive dissolution rates of pyrite*

The data presented above on the temporal evolution of aqueous and gaseous sulfide concentrations (section 3.2) was used to derive initial dissolution rates at 12 h, following the procedure for mathematical

fitting given in section 2.3.3. A summary of the mathematical fit for each experiment is provided in the supplementary section S.5. The fit quality was evaluated by the square root of the sum of squared residuals ($\sqrt{SSR}$) between the experimental and the fitted data of moles of dissolved pyrite per surface area (Eq. S.7). The residuals had values between 4.7×10^{-9} to 7.9×10^{-6} mol m^{-2} of dissolved pyrite. The final dissolution rates and modeled $pH_{in\ situ}$ values at 12 h are reported in Table 2. The dissolution rates ranged between 2.9×10^{-11} to 4.5×10^{-10} mol m^{-2} s^{-1} and showed a positive correlation with increasing T and increasing P_{H2}. Moreover, the pH-dependence of the rates showed a positive correlation with decreasing pH at acid conditions, and increasing pH at alkaline conditions.

4. Discussion

4.1. Kinetic rate law for reductive pyrite dissolution

4.1.1. Mathematical form of the rate equation

Kinetic rate laws for mineral dissolution reactions are often expressed as the product of rate-determining variables (adapted from Aagaard and Helgeson, 1982; Lasaga 1995):

$$r = k_{+}a_{H^{+}}^{-n}g(I)\prod_{i}a_{i}^{-m_i}f(\Delta G_r) \tag{7}$$

where r [mol m^{-2} s^{-1}] is the overall rate of dissolution, k_+ [mol m^{-2} s^{-1}] is the rate constant, a is the activity [unitless] of H^+-ions raised to the exponent n, $g(I)$ is the ionic strength, $\prod a_i$ is the product of all activities of i-th rate-determining species in solution that exhibit a catalytic or inhibiting effect raised to the power m_i [unitless], and $f(\Delta G_r)$ is the Gibbs free energy reaction term. An ionic strength effect was neglected in our study since we used a low 0.03 M NaCl background electrolyte concentration. The catalytic/inhibiting terms were replaced by the H_2 partial pressure raised to the power m. Thus, the general equation for the reductive dissolution rate of pyrite becomes:

$$r = k_{+}a_{H^{+}}^{-n}(P_{H_2})^{m}f(\Delta G_r) \tag{8}$$

The rate constant k_+ is defined by the Arrhenius law:

$$k_{+} = Ae^{-E_a/RT} \tag{9}$$

where A [mol m^{-2} s^{-1}] is the pre-exponential frequency factor, E_a [J mol^{-1}] is the apparent thermal activation energy, and R is the universal gas constant (8.31446 J K^{-1} mol^{-1}). The Gibbs free energy term $f(\Delta G_r)$ quantifies the degree of solution saturation with respect to the dissolving mineral as the reaction advances towards chemical equilibrium, and is therefore a rate-limiting variable (Lasaga, 1995). At far-from-equilibrium conditions, where (ΔG_r) has little or no influence on the rate, the term $f(\Delta G_r) \approx 1$ (Lasaga, 1981; 1995). Various forms of $f(\Delta G_r)$, based on different mechanisms of mineral dissolution, have been discussed in the literature (e.g., Lasaga, 1981; Burch et al., 1993; Lasaga and Lüttge, 2001; Dove et al., 2005). The most widely applied formalism is based on transition state theory (TST) (Lasaga, 1981; Aagaard and Helgeson, 1982):

$$f(\Delta G_r) = \left[1 - exp\left(\frac{\Delta G_r}{RT}\right)\right] = \left[1 - \frac{Q}{K_{eq}}\right] \tag{10}$$

where Q and K_{eq} are the ion activity product (IAP) and the equilibrium constant of the specific dissolution reaction considered. Both parameters are related to the Gibbs free energy of reaction ΔG_r [J mol^{-1}] via the following expression:

$$\Delta G_r = RT\ln\left(\frac{Q}{K_{eq}}\right) \tag{11}$$

The saturation ratio Q/K_{eq} [unitless] indicates the degree of fluid saturation with respect to the solubility of a given mineral; values < 1 indicate undersaturation and values > 1 supersaturation.

Recasting of Eqs. (9) and (10) into Eq. (8), the proposed rate law for the reductive dissolution kinetics of pyrite takes the following form:

$$r = Ae^{-E_a/RT}(a_{H^{+}})^{-n}(P_{H_2})^{m}\left(1 - \frac{Q}{K_{eq}}\right) \tag{12}$$

In geochemical modeling codes the following alternative form of the above rate equation can often be found (Marty et al., 2015):

$$r = A_{298.15}\exp\left[\frac{-E_a}{R}\left(\frac{1}{T} - \frac{1}{298.15}\right)\right](a_{H^{+}})^{-n}(P_{H_2})^{m}\left(1 - \frac{Q}{K_{eq}}\right) \tag{13}$$

Both rate equations are identical and conform to widely used geochemical codes, such as PHREEQC (Parkhurst and Appelo, 2013), CrunchFlow (Steefel, 2009), or Toughreact (Xu et al., 2006; 2011). The alternative form given in Eq. (13) will be further explained and developed in the supplementary material (Suppl. S.6).

4.1.2. Dissolution rate domains as a function of pH

The activities of the hydroxonium (H_3O^+) and hydroxide (OH^-) ions in aqueous solution change significantly with pH. Which one of these species predominates also affects the dissolution mechanism at the mineral-fluid interface. For this reason, separate rate laws are commonly derived for the acid, circumneutral, and alkaline pH domains. Within each domain, both A and E_a are generally considered to be constants (e.g., Carroll and Walther, 1990; Casey and Sposito, 1992; Hellmann, 1994). Most studies on silicate minerals show a U-shaped dependence of the dissolution rate on pH (e.g., Knauss and Wolery, 1989; Hellmann, 1994; Köhler et al., 2003; Golubev et al., 2006; Rozalén et al., 2009; Hellmann et al., 2010), which is generally mirrored by a corresponding U-shaped solubility-pH relationship (Schott et al., 2009). Regarding the sulfide pyrite, many oxidative dissolution studies concluded either no rate dependence on the H^+-ion activity (Mathews and Robins, 1974; Bailey and Peters, 1976; McKibben and Barnes, 1986; Chirita and Schlegel, 2017) or a weak linear correlation with pH (Moses et al., 1987, Williamson and Rimstidt, 1994; Domènech et al., 2002; Johnson et al., 2019). Recently Li et al. (2023) reported increasing oxidative dissolution rates at acidic and alkaline conditions, thus indicating a U-shaped pH dependence for pyrite.

Concerning the data on reductive pyrite dissolution obtained in the present study, the rates display a strong dependence on pH (Fig. 6). At least two rate-pH domains exist, defined by an asymmetric V-shaped dependence with a more pronounced increase in the rates at alkaline

Table 2
Far-from-equilibrium reductive dissolution rates (r) of pyrite evaluated at 12 h for experiments covering T, P_{H2}, and pH dependencies. The fit parameters refer to the M-M equation, Eq. (5). The $pH_{in\ situ}$ values were taken from the pyrite titration models and linearly interpolated (or extrapolated) to 12 h.

Expt #	T (°C)	P_{H2} (bar)	$pH_{in\ situ}$	r (mol m^{-2} s^{-1})	Fit parameter m	Fit parameter n
Temperature dependence:						
#PY14	60	7	9.16	2.90×10^{-11}	6.640×10^{-6}	127843.3
#PY12	90	7	8.61	4.76×10^{-11}	1.652×10^{-5}	737.5
#PY17	90	7	8.64	7.84×10^{-11}	1.248×10^{-5}	68528.9
#PY13	120	7	8.17	1.36×10^{-10}	3.150×10^{-5}	14238.5
#PY15	150	7	7.65	4.50×10^{-10}	1.056×10^{-4}	13864.4
H_2 partial pressure dependence:						
#PY18	90	20	8.57	6.24×10^{-11}	3.032×10^{-5}	395056.1
#PY23	90	50	8.47	9.01×10^{-11}	1.310×10^{-4}	1365582.1
#PY25	90	100	8.40	1.57×10^{-10}	1.137×10^{-4}	634615.9
#PY27	90	150	8.51	1.99×10^{-10}	1.842×10^{-4}	837499.7
pH dependence:						
#PY22	90	7	3.76	2.77×10^{-10}	4.783×10^{-5}	43823.6
#PY20	90	7	5.62	1.30×10^{-10}	2.283×10^{-5}	54266.8
#PY19	90	7	9.03	2.48×10^{-10}	5.101×10^{-5}	18569.9
#PY16	90	7	9.35	4.48×10^{-10}	1.623×10^{-4}	268481.3

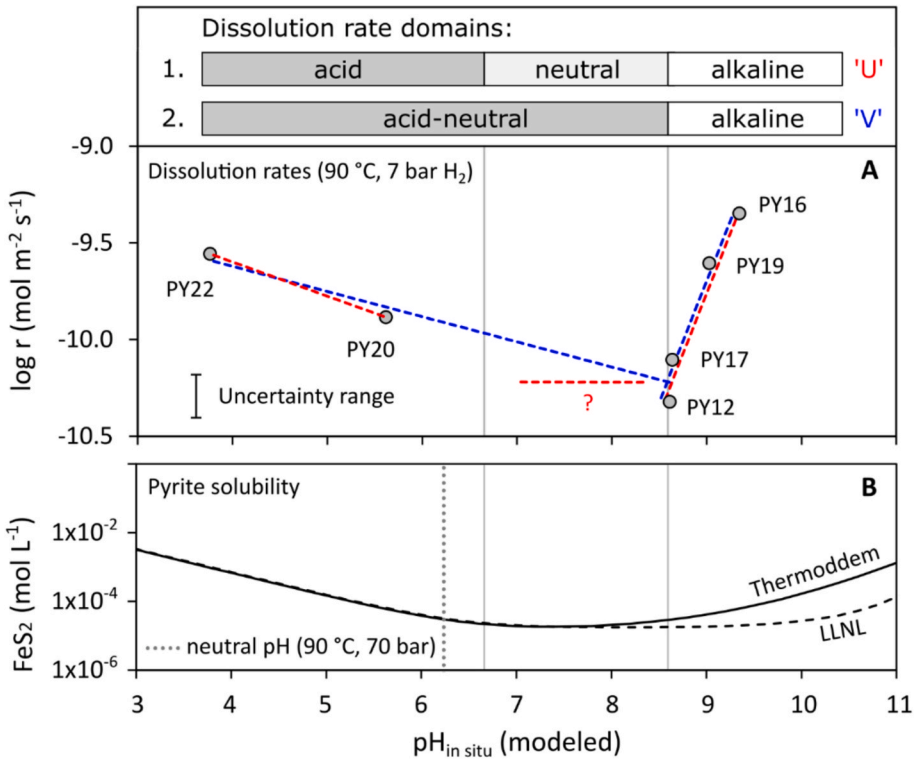

Fig. 6. Two potential interpretations of pH-dissolution rate domains based on experimental data (A) and pyrite solubility (B): 1. U-shaped pH dependence with three domains (acid, neutral, and alkaline; in red). 2. V-shaped pH dependence with two domains (acid-neutral and alkaline; in blue). A: Pyrite dissolution rates at 90 °C and 7 bar P_{H2} after 12 h of alteration as a function of the modeled $pH_{in\ situ}$. Regressions of the experimental data suggest an asymmetric V-shaped dependence of the dissolution rate on pH. The likely existence of a pH-independent circumneutral domain cannot be unambiguously constrained from the available data. The estimated uncertainty is based on the range of dissolution rates from the replicate experiments PY12 and PY17. B: Modeled solubility of pyrite at 90 °C and 7 bar P_{H2} (P_{total} = 70 bar) in 30 mM NaCl using the geochemical code PHREEQC with the Thermoddem and the LLNL databases.

versus acid pH. The lack of data in the circumneutral pH range did not allow us to unambiguously ascertain the existence of a pH-independent circumneutral dissolution rate domain. The possible existence of a neutral pH domain is nonetheless suggested by the converging regressions of the rate data at acidic and alkaline conditions (Fig. 6 A) and the U-shaped solubility of pyrite that shows minimum values over the same range (pH ~ 6-8) (Fig. 6 B).

In order to avoid tenuous conclusions, two different kinetic evaluations were performed that ultimately resulted in two different kinetic rate laws with different pH ranges of applicability. The first evaluation assumes a U-shaped dependence of the pyrite dissolution rate on pH with three separate domains defined by these approximate pH ranges: pH < 6.7 (acid), pH 6.7-8.6 (circumneutral), and > 8.6 (alkaline). The second evaluation is based on the regression of the available data and thus results in a V-shaped dependence of the dissolution rate on pH with the two approximate domains: pH ≤ 8.6 (acid-neutral) and pH > 8.6 (alkaline).

4.1.3. 1st kinetic evaluation: 'U'-shaped pH-dependence

To determine the unknown variables A, E_a, n, and m in Eq. (12), the kinetic rate data in Table 2 is used. Starting with our general rate equation, given in Eq. (8), this expression can be simplified for far-from-equilibrium rates ($f(\Delta G_r) \approx 1$) and in the pH-independent circumneutral domain ($n = 1$). Taking the logarithm of this expression results in the following equations for the three pH domains:

$$acid\,pH:\ \log r = [\log k_{+\,acid} + m\log P_{H_2}] + n_{H^+}(pH) \quad (14)$$

$$circumneutral\,pH:\ \log r = \log k_{+\,neut} + m\log P_{H_2} \quad (15)$$

$$alkaline\,pH:\ \log r = [\log k_{+\,alk} - n_{OH^-}(pK_w) + m\log P_{H_2}] + n_{OH^-}(pH) \quad (16)$$

These equations are valid only at a constant temperature, such that k_+ remains constant, as well. Equation (16) at alkaline pH was derived using the following auxiliary relations (Hellmann, 1994), where pK_w is the dissociation constant of H_2O:

$$n_{OH^-}\log a_{OH^-} = -n_{OH^-}pOH \quad (17)$$

$$pK_w = pH + pOH \quad (18)$$

In a plot of log r vs. $pH_{in\ situ}$ (Fig. 7), n corresponds to the slope of the regression of dissolution rates in each pH domain, i.e., n_{H+} = -0.18 and n_{OH-} = 1.25.

The dependence of the dissolution rate on P_{H2} was evaluated using Eq. (15). In the plot of log r vs. log P_{H2} (Fig. 8), the dissolution rates were measured in experiments at 90 °C with $pH_{in\ situ}$ values at 12 h ranging from 8.4 to 8.6. The regressed data yield a slope that corresponds to m = 0.37.

The temperature dependence of the dissolution rate was determined with the Arrhenius law, which is strictly based on rate constants (k_+) and not dissolution rates (r). The relationship between both parameters is given by rearrangement of Eq. (14), leading to:

$$\log k_+ = \log r - n(pH) - m\log(P_{H_2}) \quad (19)$$

For the pH domains considered in the 'U'-evaluation, measured values of r at variable temperatures and P_{H2} = 7 bar fall within the circumneutral pH range (except PY14, which had a slightly alkaline pH, see Table 2), such that n = 0 by definition. The log k_+ values calculated with the above equation thus considered only a P_{H2} contribution to the rate constants. The resulting k_+ values are given in Table 3 and were used in the Arrhenius law.

Taking the logarithm of the Arrhenius law as given in Eq. (20) allows

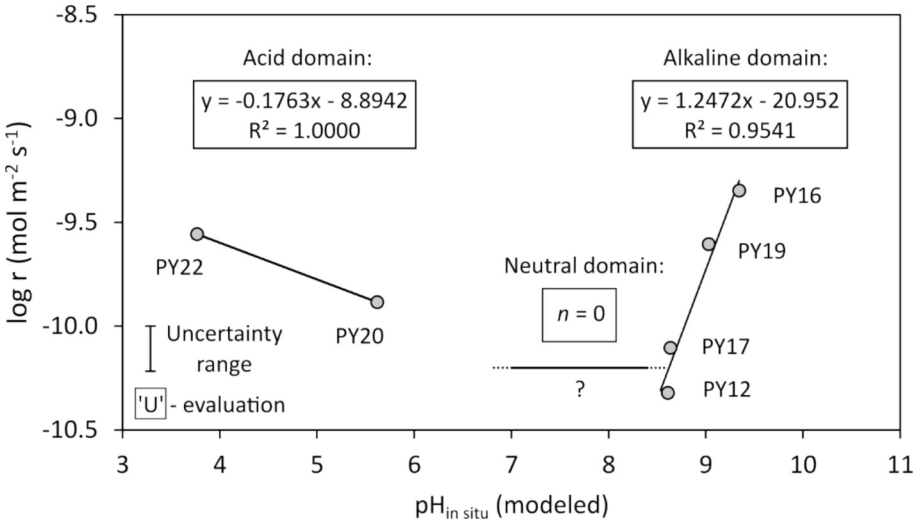

Fig. 7. Dependence of the dissolution rate of pyrite on pH at 90 °C and 7 bar P_{H2}. Regressions are based on three dissolution rate domains ('U'-evaluation), even though the neutral pH domain was not covered experimentally. The estimated uncertainty is based on the range of dissolution rates from the replicate experiments PY12 and PY17.

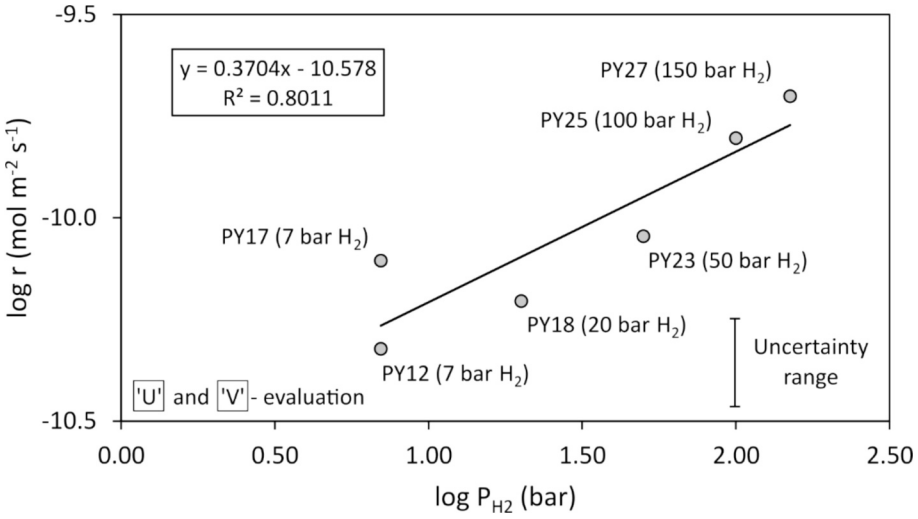

Fig. 8. Dependence of the dissolution rate of pyrite on P_{H2} at 90 °C. The regression is applicable to both the 'U' and 'V' evaluations since the impact of P_{H2} on the dissolution rate is independent of pH. The estimated uncertainty is based on the range of dissolution rates from the replicate experiments PY12 and PY17.

Table 3
Rate constants k_+ of the dissolution experiments of pyrite as a function of the temperature dependency calculated using Eq. (19). The differences in log k_+ values in the 'U' and 'V'-evaluations result from different definitions of the rate-pH domains.

			'U'-evaluation:	'V'-evaluation:
Expt #	T (°C)	log r (mol m^{-2} s^{-1})	log k_+ (mol m^{-2} s^{-1})	log k_+ (mol m^{-2} s^{-1})
#PY14	60	-10.54	-10.85	-9.66
#PY12	90	-10.32	-10.64	-9.51
#PY17	90	-10.11	-10.42	-9.29
#PY13	120	-9.87	-10.18	-9.12
#PY15	150	-9.35	-9.66	-8.66

for A and E_a to be calculated from a log k_+ vs. T^{-1} plot (Fig. 9). The y-intercept corresponds to log A = -5.42 and E_a = 35.2 kJ mol^{-1} is calculated from the slope φ of the regression using Eq. (21).

$$\log k_+ = \log A - \frac{E_a}{2.303RT} \tag{20}$$

$$E_a = -2.303\varphi R \times 10^3 \tag{21}$$

The determined value of E_a will be discussed in section 4.2 and compared with a regression of data from Truche et al. (2010), which are shown in Fig. 9.

The values of all rate-determining variables are summarized in Table 4. We did not have sufficient data to determine E_a in the acid and alkaline pH domains. Recasting into Eq. (22) gives the following expression for the dissolution rate r at circumneutral pH:

$$r = 10^{-5.42} e^{-35208/RT} (P_{H_2})^{0.37} \left(1 - \frac{Q}{K_{eq}}\right) \tag{22}$$

The above rate equation assumes that a pH-independent circumneutral rate domain does exist ('U'-evaluation).

4.1.4. 2nd kinetic evaluation: 'V'-shaped pH dependence

The determination of the rate dependencies in the presence of only two pH domains, an acid-neutral and an alkaline domain, without a pH-independent circumneutral domain ('V'-shaped rate-pH relation), is

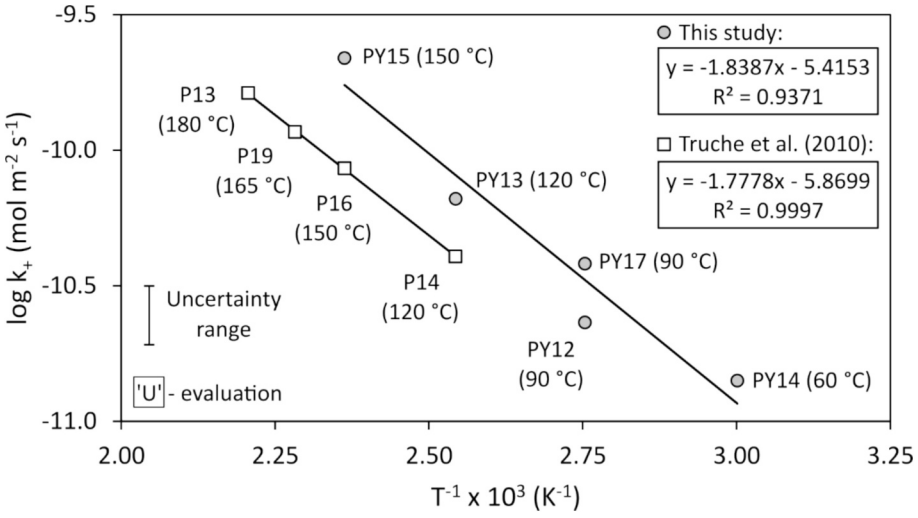

Fig. 9. Dependence of the rate constant k_+ of pyrite dissolution at circumneutral pH on temperature. The data from Truche et al. (2010) was newly evaluated according to the workflow in this study. The regressions are based on the existence of a circumneutral rate-pH domain ('U'-evaluation). The estimated uncertainty is based on the range of dissolution rates from the replicate experiments PY12 and PY17.

Table 4
Values of rate parameters for the reductive dissolution of pyrite following two evaluation strategies that assume either three ('U') or two ('V') dissolution rate-pH domains. n.d. = not determined.

Rate-pH evaluation:	'U'-shaped pH-dependence			'V'-shaped pH-dependence	
pH domain	Acid	Neutral	Alkaline	Acid-neutral	Alkaline
n	-0.18	0	1.25	-0.13	1.25
m	0.37	0.37	0.37	0.37	0.37
log A (mol m^{-2} s^{-1})	n.d.	-5.42	n.d.	-5.13	n.d.
E_a (J mol^{-1})	n.d.	35 208	n.d.	29 370	n.d.

analogous to but numerically slightly different from the evaluation in section 4.1.3. In this case, the rates of PY12 and PY17 are included in both the acid-neutral and alkaline pH regressions (Figs. 6, 10). In the alkaline domain, the dependence of the dissolution rate on pH and P_{H2} remains identical to the 'U'-evaluation, such that $n_{OH^-} = 1.25$ and $m = 0.37$. The pH exponent in the acid-neutral domain changes to $n_{H+} = -0.13$.

The temperature dependence of the dissolution rate is evaluated using the same values of r at $P_{H2} = 7$ bar, as in section 4.1.3. These fall within the acid-neutral pH range (except PY14), such that in the 'V'-evaluation n ≠ 0 in Eq. (19). For the calculated k_+ values given in Table 3, the pH and P_{H2} contributions are thus considered, unlike in the 'U'-evaluation. The determined values of the Arrhenius parameters are $E_a = 29.4$ kJ mol^{-1} and log $A = -5.13$ (Fig. 11).

Recasting the values of the rate dependencies into Eq. (23) gives the following expression for the dissolution rate r in the acid-neutral pH range:

$$r = 10^{-5.13} e^{-29370/RT} (a_{H^+})^{0.13} (P_{H_2})^{0.37} \left(1 - \frac{Q}{K_{eq}}\right) \quad (23)$$

The above rate equation assumes that a pH-independent circumneutral rate domain does not exist ('V'-evaluation).

4.2. Interpretation and comparison of the apparent activation energy

The accurate quantification of E_a in batch reactor studies can have unforeseen complexities. As E_a is derived from the slope in the Arrhenius

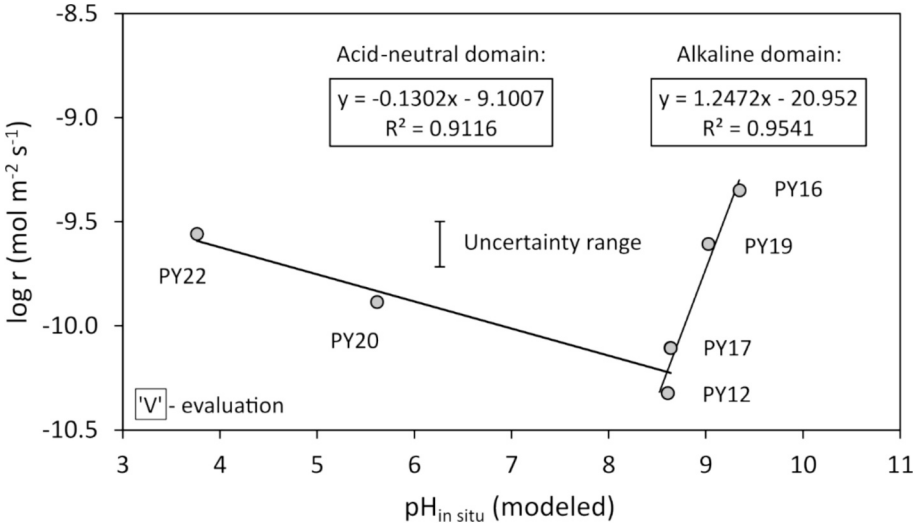

Fig. 10. Dependence of the dissolution rate of pyrite on pH at 90 °C and 7 bar P_{H2}. The two regressions are based on two dissolution rate-pH domains ('V'-evaluation). The estimated uncertainty is based on the range of dissolution rates from the replicate experiments PY12 and PY17.

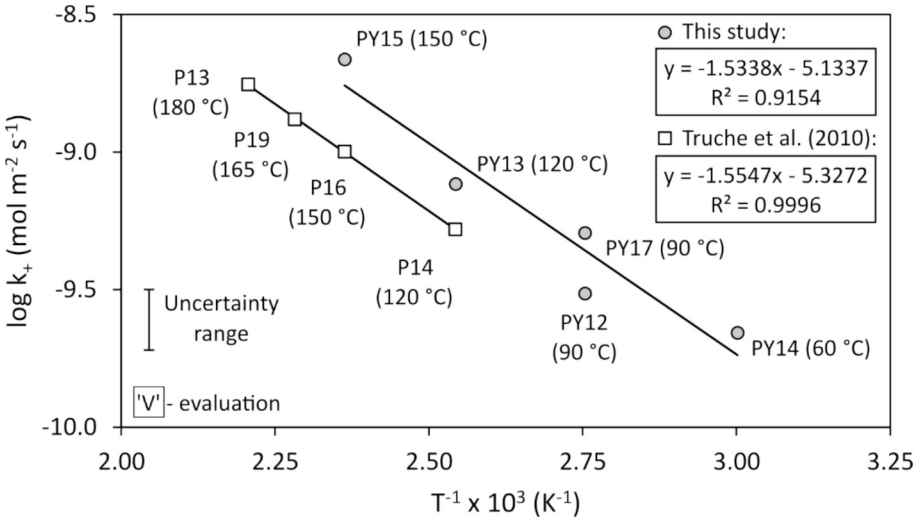

Fig. 11. Dependence of the rate constant k_+ of pyrite dissolution on temperature. Data from Truche et al. (2010) was newly evaluated analogously to the workflow in this study. The regressions are based on the absence of a circumneutral rate-pH domain ('V'-evaluation). The estimated uncertainty is based on the range of dissolution rates from the replicate experiments PY12 and PY17.

plot, its value is affected by the calculation of the rate constants k_+ from the measured dissolution rates. The rates are in turn influenced by all parameters indicated in the general rate equation (Eq. (7)), and not just temperature. Moreover, some experimental parameters, such as pH or the water/rock ratio, continuously change in batch reactor systems and thus additionally influence the measured rates via the Gibbs free energy (Nagy and Lasaga, 1992; Cama et al., 1999). For example, the difference in E_a between the 'U' (35.2 kJ mol^{-1}) and 'V'-evaluations (29.4 kJ mol^{-1}) in our study only originates from the different pH contribution to the k_+ values in both cases, despite being based on exactly the same rates (sections 4.1.3, 4.1.4).

The determined E_a values for H_2-driven pyrite reduction in the present study can be compared with that from Truche et al. (2010). Using a similar batch reactor setup as we did, these authors determined that E_a = 53 kJ mol^{-1}. We re-evaluated the 120-180 °C, 8 bar P_{H2} data of Truche et al. (2010), following the same protocol applied in our study (Table 5). The rate constants derived from the re-evaluated data are plotted in the Arrhenius diagrams (Figs. 9, 11) and yield E_a = 34.0 kJ mol^{-1} ('U'-evaluation) and 29.8 kJ mol^{-1} ('V'-evaluation). Interestingly, Rickard and Luther (1997) published an E_a value of 33.7 kJ mol^{-1} for the sulfidation of pyrrhotite by H_2S, i.e., the inverse reaction to the dissolution of pyrite by H_2. These values are nearly the same as those determined from our own experimental data.

The E_a value is often interpreted in terms of the reaction mechanism (Lasaga and Gibbs, 1990). Two end-member cases are distinguished: transport-controlled reactions of soluble minerals with corresponding E_a values < 21 kJ mol^{-1} and surface-controlled reactions of insoluble minerals with E_a between 42-84 kJ mol^{-1} (Berner, 1978; Lasaga, 1984). The pyrite E_a values determined above fall between both limiting cases. However, the dissolution process and associated rates can be a complex function involving both transport and surface kinetic steps (Lasaga, 1998). Either one can be rate-limiting depending on the physicochemical conditions (Berner, 1978).

The above example emphasizes the significant impact of data treatment on the E_a value. Conclusions about the reaction mechanism should therefore not only be based on the interpretation of the activation energy, but require complementary physical and chemical observations at different scales (Lasaga and Lüttge, 2004; Lüttge, 2006).

4.3. Rate dependence on Gibbs free energy and the far-from-equilibrium criterion

The dissolution rate of any mineral must decrease as the fluid composition evolves from far-from-equilibrium conditions ($\Delta G_r = -\infty$) to the chemical equilibrium state ($\Delta G_r = 0$). Even though numerous studies have investigated the rate evolution as a function of Gibbs free energy (r-ΔG_r), there is no consensus on the mathematical form and the controlling mechanism. The commonly used TST-formalism postulates the existence of an extensive rate plateau, that abruptly ends with a sharp rate decline close to equilibrium, terminating at $r = 0$ at $\Delta G_r = 0$ (Lasaga, 1981; Aagaard and Helgeson, 1982). However, the TST-rate prediction has been questioned by several experimental (e.g., Nagy and Lasaga, 1992; Burch et al., 1993; Taylor et al., 2000; Beig and Lüttge, 2006; Hellmann and Tisserrand, 2006; Hellmann et al., 2010) and theoretical studies (Lüttge, 2006; Lüttge et al., 2019), based on the existence of a sigmoidal r-ΔG_r relation characterized by: *i)* a ΔG_r-independent rate plateau at far-from-equilibrium, *ii)* a transition region with fast decreasing rates, and *iii)* a near-equilibrium region with slowly decreasing rates extending to $\Delta G_r = 0$. This non-linear evolution of r-ΔG_r is postulated to be governed by the energetics of dislocation defects. The sigmoidal transition corresponds to an energy threshold ($\Delta G_{r,\,crit}$) and a concomitant change in mechanism (Burch et al., 1993; Lasaga and

Table 5
Re-evaluated data from temperature experiments reported in Truche et al. (2010) following the data treatment and both kinetic evaluations ('U' vs. 'V') applied in the present study. The fit parameters refer to the M-M equation, Eq. (5). The rates (log r) and the rate constants (log k_+) are given in [mol m^{-2} s^{-1}].

Expt #	T (°C)	P_{H2} (bar)	at 12 h		Fit parameters		'U'-eval.	'V'-eval.
			corrected $pH_{in\ situ}$	log r	m	n	log k_+	log k_+
#P14	120	8	8.53	-10.06	1.554×10^{-5}	59791.9	-10.39	-9.28
#P16	150	8	8.21	-9.73	5.089×10^{-5}	178485.2	-10.07	-9.00
#P19	165	8	8.08	-9.60	4.986×10^{-5}	91235.9	-9.93	-8.88
#P13	180	8	7.95	-9.46	6.255×10^{-5}	30017.4	-9.80	-8.76

Lüttge, 2001; Lüttge, 2006).

In order to address the influence of ΔG_r on the pyrite dissolution rates measured in our batch experiments, r-ΔG_r plots for the T and P_{H2}-series experiments were constructed (Fig. 12, data in Suppl. S.8). For this purpose, additional rates were derived with a Michaelis-Menten fit over the full experimental duration of each experiment. The ΔG_r at each sampling step was calculated using Eq. (24), that was derived by substituting ln (Q/K_{eq}) in Eq. (11) by the SI_{FeS2}.

$$\Delta G_r = RT \times SI_{FeS_2} \times \ln 10 \quad (24)$$

The SI_{FeS2} values were extracted from the PTMs. The values of ΔG_r therefore correspond to the dissolution reaction of pyrite as defined in the Thermoddem database:

$$FeS_2 + 0.75H_2O = Fe^{2+} + 1.5HS^- + 0.25S_2O_3^{2-} \quad (25)$$

This reaction stoichiometry can be converted into the reductive dissolution reaction of pyrite by H_2 (Eq. (1)) as a linear combination of other speciation reactions (Suppl. S.8).

Published mineral dissolution rates and derived kinetic rate laws are commonly based on far-from-equilibrium rates and use the TST-based $f(\Delta G_r)$ term as the rate-limiting parameter. For these reasons, we posed two principal questions that were evaluated with the r-ΔG_r plots in Fig. 12. First, do the instantaneous rates determined at 12 h in our batch reactor system represent far-from-equilibrium conditions? Second, do the experimental rates deviate from the predicted rates of the TST-formalism?

Only the low reactivity experiments at 60 °C and 90 °C at 7 bar P_{H2} show significantly decreasing dissolution rates with increasing ΔG_r. This trend is already evident close to the beginning of the experiments (Fig. 12 A). An influence of the dissolution rate at 12 h by ΔG_r therefore cannot be excluded at these conditions. But for all other experiments at $\geq$ 120 °C and P $\geq$ 20 bar H_2 (Fig. 12 B), rate decreases with increasing ΔG_r occur only at later time steps, such that an impact of ΔG_r on the dissolution rates seems unlikely.

Interestingly, the different r-ΔG_r trends of the T and P_{H2}-experiments in Fig. 12 correlate with the observed differences in secondary pyrrhotite abundance (section 3.1) and measured dissolved sulfide concentrations (Figs. 3, 4). The experiments with nearly no secondary pyrrhotite formation (PY12, PY14 PY17, PY18) show rapidly decreasing rates with increasing ΔG_r, that match the transition region of a sigmoidal r-ΔG_r trend. The rates in these experiments deviate from the TST-rate curve by up to three orders of magnitude. However, with increasing T, P_{H2}, and pyrrhotite precipitation, the r-ΔG_r slopes progressively flatten. This leads to the impression of an apparent shift of $\Delta G_{r,\,crit}$ to higher ΔG_r values, i.e., a shift of the inflection point between the rate plateaus and the transition regions. At 120 °C and 150 °C this apparent shift is so pronounced (Fig. 12 A), such that the r-ΔG_r trends resemble the TST-rate curves.

We note here that ΔG_r continuously changes in batch reactors as a temporal function of the fluid saturation with respect to the dissolving mineral ($Q/K_{eq} \rightarrow 1$). Secondary mineral formation, changing pH, and decreasing water/rock ratio consequently impact the ΔG_r and the dissolution rates, either directly or indirectly via the SI_{FeS2}. In addition, abundant etch pits, indicative for rate-controlling screw dislocations, were commonly observed in our experiments. These form at high solution undersaturation on the rate plateau but remain active in the transition zone and may artificially lead to enhanced rates (Lüttge, 2006).

The r-ΔG_r relations in Fig. 12 should therefore be evaluated with caution, in particular for experiments with significant secondary mineral formation (e.g., PY13, PY15, PY27). Pyrrhotite and magnetite precipitation lead to elevated measured dissolution rates by lowering the IAP_{FeS2}, such that true r-ΔG_r relations cannot be determined. The extended 'rate plateaus' in such experiments are therefore most likely artifacts. The least impacted r-ΔG_r relations are therefore considered to

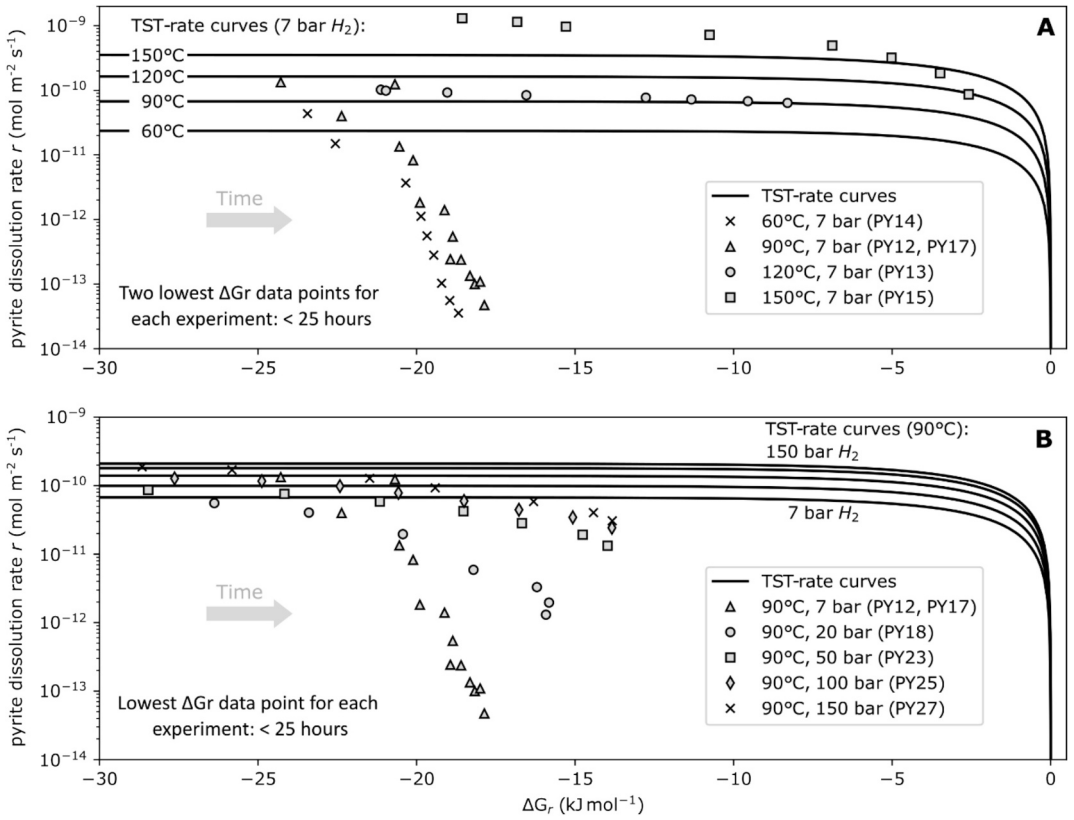

Fig. 12. Rates of pyrite reductive dissolution for all temperature experiments (A) and experiments at variable partial pressure of H_2 (B) as a function of ΔG_r, compared to calculated rate curves using the overall rate expression based on the 'U'-evaluation, Eq. (22).

be the low-reactivity experiments with nearly no secondary mineral formation (PY12, PY14, PY17). These show complex, non-linear r-ΔG_r relations for pyrite that significantly deviate from the TST-law, suggesting that TST is not universal for all minerals.

We question whether in batch reactor systems instantaneous rates determined from a concentration vs. time curve are true steady-state rates at a given ΔG_r value? Although all experimental systems can be deleteriously impacted by the effect of secondary mineral precipitation, r-ΔG_r relations are arguably better determined in continuous flow reactor systems that generate steady-state rates at constant ΔG_r values (Q/K_{eq} = const.). We note, however, that the investigation of the r-ΔG_r relation for the reductive dissolution of pyrite was not the primary objective of this study. Moreover, conducting H_2-driven aqueous mineral dissolution experiments in flow-through systems can lead to significant additional complexity due to the requirement for a constant H_2-activity in solution, safety precautions, and lower sulfide concentrations.

4.4. Performance of the kinetic rate laws

Both rate laws ('U' and 'V'-evaluations; Eqs. (22), (23)) were validated by reproducing the experimentally measured dissolved sulfide concentrations. To this aim, they were implemented in the Thermoddem database and the reductive dissolution of pyrite by H_2 modeled kinetically using PHREEQC. To achieve a match with the experimental data, the suppression of pyrrhotite and magnetite precipitation was required, but only for the models concerning the low-reactivity experiments ($\leq$ 90 °C and $\leq$ 20 bar P_{H2}, with $S^{II}_{(aq)} < 0.12$ mM: PY14, PY17, PY18, PY20, PY22). This is in line with the sparse abundance of secondary phases observed on post-reaction grains in the SEM examination of these experiments (section 3.1). The application ranges of both rate laws with respect to T, P_{H2}, and pH are given in section 4.4.2.

4.4.1. Kinetic modeling of the experiments

To graphically illustrate the performance of the kinetic models relative to the experiments, modeled concentration vs. measured concentration plots are shown in Fig. 13. Two comparisons are performed. First, the 'U' and 'V' rate laws are compared and second, their match with the experimental reference data. The divergences of both rate laws and their agreement with the experimental data is given in Table 6. In addition, the temporal evolution of the modeled and measured sulfide concentrations is evaluated, for example, in Fig. 14 with respect to P_{H2} at experimental time scales and then extended to 10 000 h. The temporal evaluation for all other experiments is presented in the supplementary material (Suppl. S.7).

In general, the modeled sulfide concentrations using the 'U' and 'V' kinetic rate laws are nearly identical over experimental time-scales for variable T and P_{H2} conditions, as shown in Fig. 13. The most notable divergences occur for the pH-series experiments, which is due to the missing rate dependence on pH in the 'U' rate law. The zig-zag excursions from non-monotonic behavior in some of the concentration vs. concentration plots (Fig. 13, e.g., PY14, PY17, PY20) are related to the missing time component. They occur in particular in low-reactivity experiments due to successive positive and negative measured sulfide fluctuations at (near)-steady-state conditions relative to the ideal modeled trends.

For most conditions, the 'U' and 'V' curves conform well (within ~ 20 %) with the corresponding experimental reference curves. Two exceptions are highly alkaline conditions (pH > 10, Fig. 13 PY16) that could not be reproduced, and temperatures $\geq$ 120 °C with deviations $\geq$

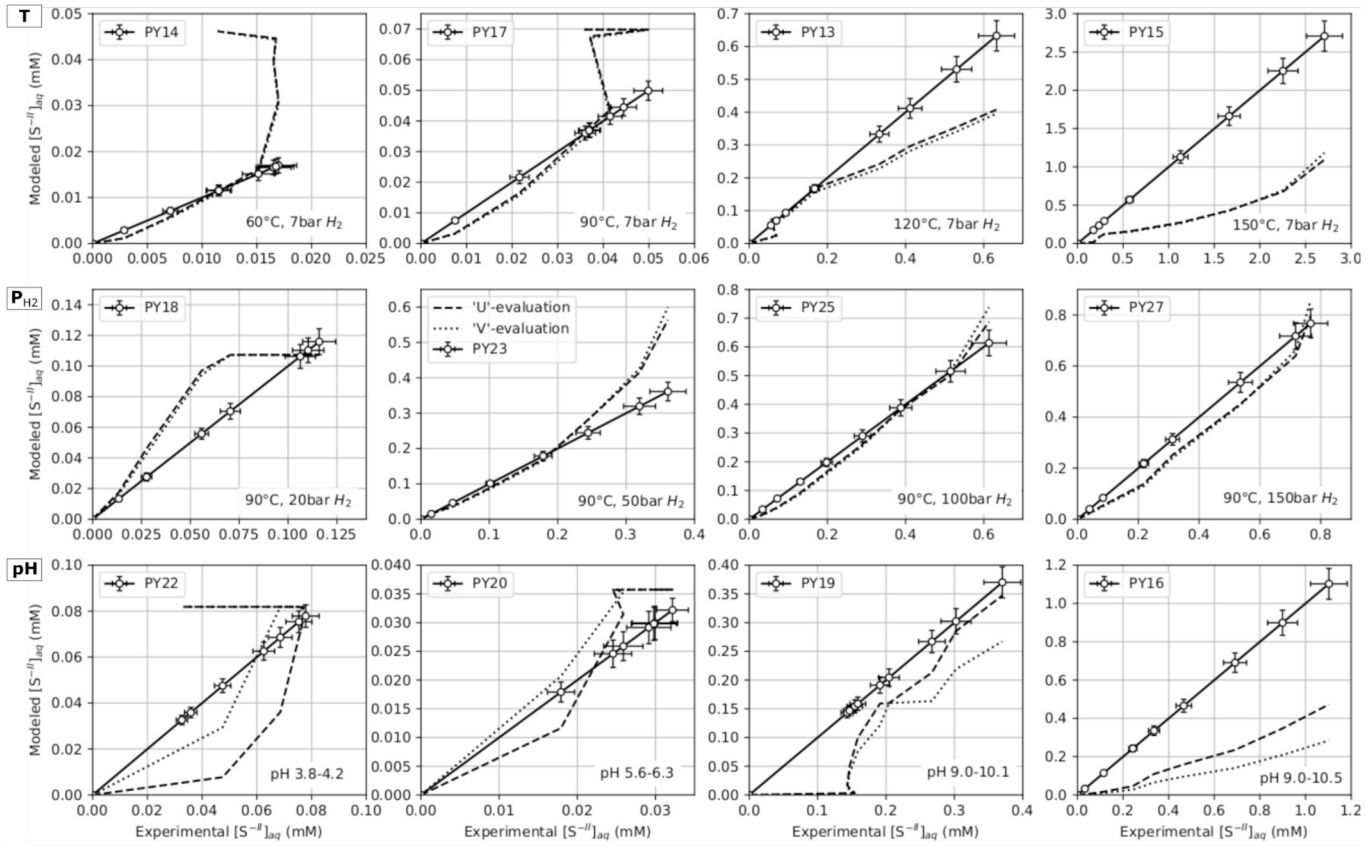

Fig. 13. Performance test of the rate laws. Comparison of the kinetically modeled dissolved sulfide concentrations, $[S^{-II}]_{(aq)}$, with the measured concentrations by methylene blue spectrophotometry. The reference curve for each experiment (solid line) displays the same values on ordinate and abscissa. The legend given for PY23 is applicable to all plots.

Table 6
Summarized comparison of the 'U' and 'V' rate laws and their performance with respect to the T, P_{H2}, and pH conditions of experiments.

Experimental conditions:	Comparison between the 'U' and 'V' rate law models:	Agreement with experiments:	Remarks:
Acidic pH (< 6.7)	'U': no pH dependence; lower initial sulfide release 'V': pH dependence included	'U' and 'V' converge with peak conc. (PY22: 5 %, PY20: 11 %) 'V': More accurate	Recommended use: 'V' rate law
Alkaline pH (> 8.6)	Missing E_a and A thermal parameter values	pH ~ 9-10 (PY19): 'U'- within ~ 20 % pH > 10 (PY16): not reproducible	'U' and 'V' rate laws not applicable except at 90 °C (section 4.4.2; not tested)
Temperature (≤ 90 °C)	Very similar trends and steady-state conc. (≤ 6 %)	Accurate trends; overestimated steady-state conc. by 0.02-0.03 mM	Overestimated near-equilibrium rates caused by the TST-based $f(\Delta G_r)$ term (section 4.3)
Temperature (≥ 120 °C)	Similar short and long-term conc. (≤ 10 %)	Exp. time-scale: Underestimation (≥ 30 %, 120 °C; > 50 %, 150 °C) Ext. time-scale (10k h): Plausible trends	Recommended range of application: max. ~ 120 °C Elevated analytical uncertainty (MB-spectrophotometry)
H_2-pressure (≤ 150bar)	Exp. time-scale: Similar conc. (≤ 9 %) Ext. time-scale (10k h): 'V' at P_{H2} > 100 bar: 1-2 mM higher conc.	Overall agreement within ~ 20 %	Long-term differences between 'U' and 'V' due to pH effect

30 % (Fig. 13 PY13, PY15). The deviations from the experimental measurements at 150 °C may in part be related to overestimated concentrations by methylene blue analysis at millimolar range of concentrations. At these conditions, the methylene blue measurements also deviate from the $S^{-II}_{(aq)}$ estimates by potentiometry and SO_4^{2-}-conversion to higher concentrations (Fig. S.5-4a). Nevertheless, over time scales up to 10 000 h, both rate laws predict reasonable steady-state sulfide concentrations of 2.6 mM (120 °C) and 4.3 mM (150 °C) (Fig. S.7-1b C, Fig. S.7-2b C). In contrast, the experiments at high $P_{H2} \geq 100$ bar and 90 °C, conditions most relevant to UHS, were reproduced well by both rate laws (Fig. 14). Only the two lower P_{H2} experiments show slight deviations from the experimental data, a transitory initial deviation at 20 bar P_{H2} (Fig. 13 PY18) and a positive deviation at the end of the experiment at 50 bar P_{H2} (Fig. 13 PY23).

Figure 14 illustrates another difference between the experiments and the kinetic models, specifically regarding the time scale over which the dissolution rates start to significantly slow down. The dissolved sulfide concentrations in the experiments begin to flatten out within ~ 1 000 h (Fig. 14 A, Fig. S.7-1b A), whereas linearly increasing concentrations are predicted by the models over the same time scale. The modeled rates of sulfide accumulation start to significantly decrease over much longer time periods (Fig. 14 B, Fig. S.7-1b C). This implies a discrepancy between the models and experiments concerning the impact of the pyrite saturation state with respect to limitation of the dissolution rate. One explanation is overestimated rates near equilibrium by the TST-based ΔG_r term in the rate equations (section 4.3). Another explanation is that the models do not consider the nucleation and growth kinetics of pyrrhotite and magnetite. The effect of instantaneous precipitation on fluid saturation results in overly efficient removal of Fe^{+II} and $S^{-II}_{(aq)}$. As a consequence, the undersaturation of pyrite is overestimated and artificially prolonged.

4.4.2. *Application range of the kinetic rate laws*

The valid range of our rate laws is more restricted than the experimentally investigated T, P_{H2}, and pH conditions. In terms of T and P_{H2}, the performance analysis of both rate laws (section 4.4.1) suggests significant deviations from the experiments at 150 °C. Therefore, we recommend a suitable range of application from 60 °C to ~ 120 °C, with an unrestricted P_{H2} range up to 150 bar. Conversely, the incompleteness of the rate data sets with respect to their temperature dependence resulted in undeterminable Arrhenius parameters (E_a and A) in the acid and alkaline pH domains (section 4.1.3-4.1.4). This restricts the validity of the 'U' rate law to the circumneutral domain from pH ~ 6.7 to 8.6 and the 'V' rate law to the acid-neutral domain extending from pH ~ 4.1 to 8.6. In the other pH domains, the rate laws are only valid at a constant temperature of 90 °C and necessitate the use of a fixed k_+ value each (acid domain ('U'): log k_+ = -9.19 ± 0.01 mol m^{-2} s^{-1}; alkaline domain ('U', 'V'): log k_+ = -21.29 ± 0.10 mol m^{-2} s^{-1}), that is derived by Eq. (19) from the corresponding experiments. Because E_a is known to vary with the pH domain, it is not advisable to use the determined E_a values outside of their valid pH conditions.

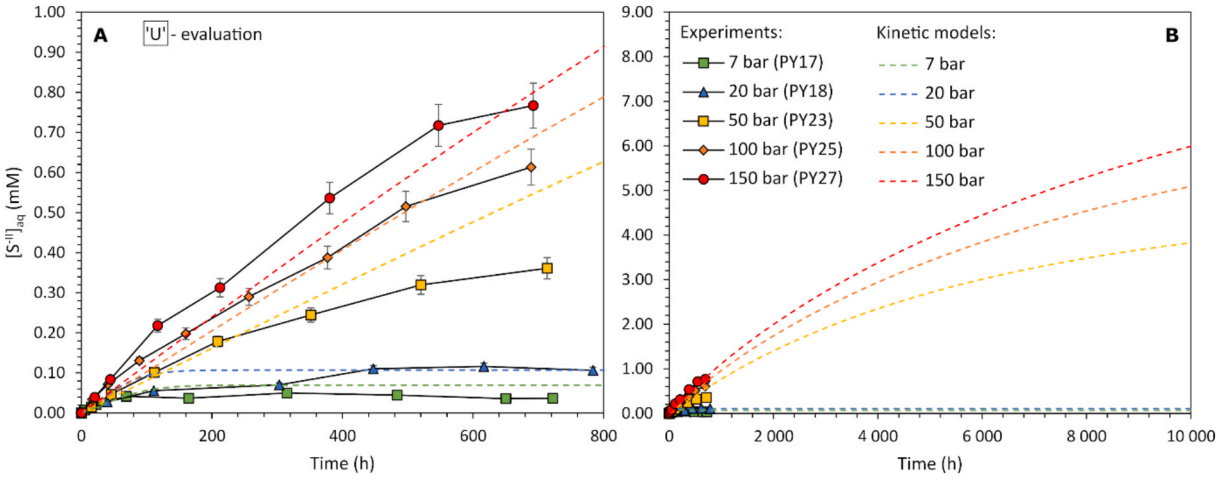

Fig. 14. Experimentally measured vs. modeled dissolved sulfide concentrations for the 'U' kinetic rate law for variable P_{H2} at 90 °C. A: Experimental time scale. B: Extended time scale.

4.5. Implications for aqueous pyrite reduction

4.5.1. Control of reductive pyrite dissolution by mineral solubilities

The longevity of sulfide production by H_2-driven pyrite dissolution is a function of mineral solubilities that control the saturation state of pyrite. Regarding pyrite, pyrrhotite, and magnetite, the order of mineral solubilities at acidic and alkaline conditions is inversed (Fig. 15), in agreement with the pyrite-H_2 reaction regimes suggested by Truche et al. (2013). At acidic conditions, pyrite saturates first because it has the lowest solubility. In this case pyrrhotite remains undersaturated, such that dissolved sulfide concentrations are governed by the solubility of pyrite that rapidly equilibrates with the fluid without secondary mineral formation (e.g., PY22; Fig. 1 I). At circumneutral to alkaline conditions, pyrrhotite has a lower solubility than pyrite and thus saturates first, albeit eventually after magnetite (see section 4.5.2). When pyrrhotite forms, the dissolution regime is driven by scavenging of Fe^{+II} and $S^{-II}_{(aq)}$ which keeps the IAP_{FeS2} low and results in long-term pyrite dissolution and pyrrhotite growth (e.g., PY19; Fig. 1 K). Given that for each mole of dissolved pyrite an excess of $S^{-II}_{(aq)}$ relative to Fe^{+II} is released as given in Eq. (1), the solution remains Fe-depleted, if pyrrhotite precipitates. This also implies that the amount of secondary pyrrhotite formation is constrained by the amount of available Fe in solution during pyrite dissolution. Significant dissolved Fe was therefore only measured in the acidic experiments, where pyrrhotite saturation was not achieved (PY22) or where pyrrhotite precipitation was minimal (PY20). Similarly, magnetite also affects the saturation state of pyrite by the incorporation of Fe^{+II}.

4.5.2. Oxidation and magnetite formation

The formation of magnetite can be considered to be unexpected in deoxygenated, H_2-bearing experiments at reducing conditions. However, the solubility relations at alkaline conditions indicate that the saturation of magnetite is achieved prior to pyrrhotite and pyrite (Fig. 15). The observation of magnetite precipitation in our circumneutral to alkaline experiments at low P_{H2} (e.g., PY12-17, PY19) therefore indicates that the oxidation of Fe^{+II} to Fe^{+III} occurs, and is most likely due to residual traces of dissolved $O_{2(aq)}$. Despite the application of inert gas purging, which is considered an efficient deoxygenation technique, residual concentrations of ~ 0.01-0.03 mM $O_{2(aq)}$ commonly remain in solution (Butler et al., 1994; Zekos and Stack, 2019). We assume that magnetite formation would not occur, if the experimental solutions were completely O_2-depleted from the beginning. However, achieving truly O_2-free starting conditions without alteration of the chemistry of the experimental solutions would be difficult at best. As a consequence, residual $O_{2(aq)}$ in our experimental solutions may actually be reduced by magnetite precipitation, before pyrrhotite starts forming.

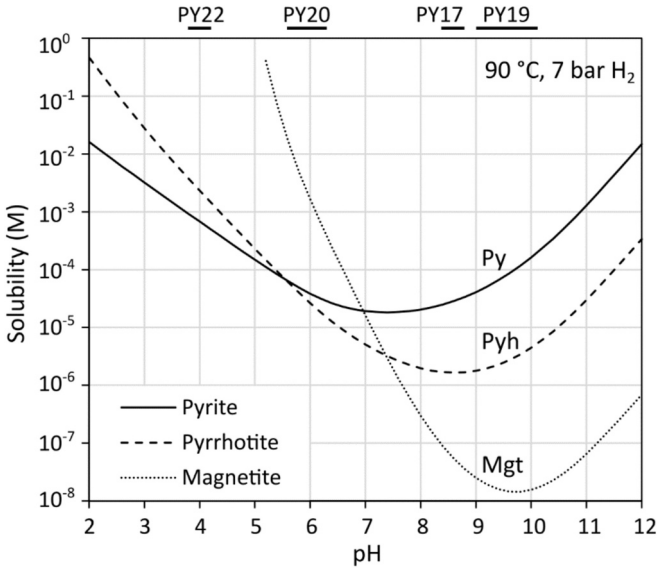

Fig. 15. Modeled solubilities of pyrite, pyrrhotite, and magnetite as a function of pH at 90 °C and 7 bar P_{H2}. The in situ pH ranges of select experiments are indicated at the top of the diagram. With increasing temperature, the solubility curves shift to lower pH, but maintain a similar topology. With increasing H_2 partial pressure, the solubility curves of pyrite and magnetite shift to higher values, while the solubility of pyrrhotite remains unaffected.

4.5.3. Pyrite dissolution stoichiometry (Fe/S^{-II}-ratio)

The dissolution stoichiometry of pyrite is not preserved by the solution composition because $Fe_{(aq)}$ and $S^{-II}_{(aq)}$ do not behave conservatively due to devolatilization and scavenging by secondary mineral formation processes. The temporal evolution of the Fe/S^{-II}-ratio is given in Fig. 16, where a value of 0.5 represents stoichiometric dissolution of pyrite. For experiments PY19 and PY27 the ratios are < 0.5 due to dissolved Fe concentrations near the detection limit. However, if the number of moles of pyrrhotite formation, estimated by the PTMs, are considered in the mole balance for total S^{-II}, an Fe/S^{-II}-ratio of 0.50 ± 0.03 is obtained, indicating the congruent dissolution of pyrite in the presence of H_2. In the other circumneutral to alkaline experiments, the measured dissolved Fe concentrations fluctuate around the detection limit by ICP-OES, such that the ratio could not be calculated. The acidic experiments PY20 and PY22, which were undersaturated with respect to pyrrhotite, show measured dissolved Fe concentrations that exceed the total $S^{-II}_{(aq+gas)}$ production, hence leading to Fe/S^{-II}-ratios > 0.5. Trace abundances of Fe-bearing inclusions in the pyrite starting material are suspected as the cause of the elevated Fe signal (e.g., Suppl. section S.1-2).

4.5.4. Pyrite-pyrrhotite-magnetite sulfide buffer assemblage

When the minerals pyrite, pyrrhotite, and magnetite coexist in the kinetic models (section 4.4.1), the sulfide concentration is buffered (e.g., Fig. S.7-1b B). The buffering effect of this mineral assemblage on $S^{-II}_{(aq)}$ concentrations is known from other studies on hydrothermal systems (Crerar, 1978; Kishima et al., 1989). In our experiments, with continued sulfide release the solution becomes undersaturated with respect to magnetite, this leading to the instability (i.e., termination) of the buffer assemblage and a renewed increase in $S^{-II}_{(aq)}$ concentrations. This was observed by the early-stage intervals (~ 30-80 h) of transient slower sulfide release kinetics in the experiments at 120 °C (PY13) and 150 °C (PY15) described in section 3.2.1. The same effect is also predicted for the experiment at pH ~ 9.7, PY19 (Fig. S.7-1c B).

5. Conclusions

Relative to other geologic environments, underground H_2 storage is unique in terms of abiotic redox reactions, because low temperature conditions are accompanied by high H_2 partial pressures. To investigate the dependence of the reductive dissolution rate of pyrite at conditions relevant to UHS, powder dissolution experiments were performed in H_2-pressurized batch reactors as a function of T (60-150 °C), P_{H2} (max. 150 bar), and pH (~ 4-10). The experiments showed that the reductive dissolution rates of pyrite are not only a strong function of T, but also significantly increase with P_{H2} and pH at alkaline conditions. Sulfide formation was measured at temperatures as low as 60 °C (7 bar P_{H2}) and rates even increased slightly from neutral to acidic pH (90 °C, 7 bar P_{H2}), albeit at low sulfide release (10^{-6} to 10^{-5} mol m^{-2} $S^{-II}_{(aq+gas)}$). Long-term aqueous pyrite reduction and concomitant elevated sulfide release (10^{-4} to 10^{-3} mol m^{-2} $S^{-II}_{(aq+gas)}$) at conditions ≥ 120 °C (7 bar P_{H2}) or ≥ 50 bar P_{H2} (90 °C) are driven by the saturation and precipitation of secondary pyrrhotite and magnetite.

In this study, two general kinetic rate laws were derived, based on different rate-pH domains. The validity of both rate laws was satisfactorily confirmed in kinetic models by reproducing the experimentally measured dissolved sulfide concentrations and mineralogical changes at 60-120 °C and up to 150 bar P_{H2}. However, their application is restricted

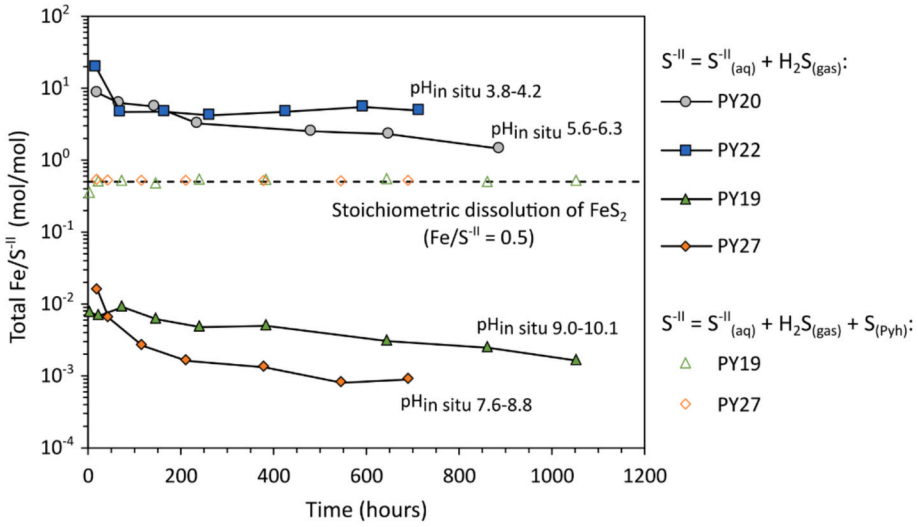

Fig. 16. Temporal evolution of the total Fe/S^{-II} ratio for experiments with a detectable Fe concentration by ICP-OES. The total sulfide balance (S^{-II}) includes dissolved sulfide measured by methylene blue spectrophotometry ($S^{-II}_{(aq)}$), gaseous H_2S based on the PTMs, and sulfide in secondary pyrrhotite, also derived from the PTMs ($S_{(Pyh)}$). For experiments PY19 and PY27 two sulfide balances are shown, one excluding and one including $S_{(Pyh)}$, thereby illustrating the impact of Fe and $S^{-II}_{(aq)}$-scavenging by pyrrhotite precipitation.

to specific pH ranges, for which the *T*-dependence could be fully developed. The first rate law, Eq. (22), assumes a U-shaped dependence of the pyrite dissolution rate on pH and incorporates the *T*-dependence (E_a = 35.2 kJ mol^{-1}) in the circumneutral range of pH ~ 6.7-8.6. The second rate law, Eq. (23), is based on a V-shaped rate dependence on pH and accounts for the *T*-dependence (E_a = 29.4 kJ mol^{-1}) in the acid-neutral range of pH ~ 4.1-8.6. More *T*-experiments are required to establish the activation energies in the acid and alkaline pH domains.

Additional analyses of the rate dependence on the Gibbs free energy suggest that the TST-based ΔG_r term leads to overestimated dissolution rates close to equilibrium. This appears to be a systematic limitation in TST-based rate laws (e.g., Nagy and Lasaga, 1992; Burch et al., 1993; Hellmann and Tisserrand, 2006; Lüttge, 2006), whose usage in large-scale geochemical simulations currently seems to be unavoidable, however (Marty et al., 2015).

Despite these caveats, the rate data provided in this study allow for the quantitative prediction of abiotic sulfide release rates from H_2-driven pyrite reduction in future reactive transport models. This work therefore supports the study of water-rock interactions, long-term safety assessments, and techno-economic planning of engineered subsurface sites that will be used for underground H_2 storage, carbon capture and storage, and nuclear waste disposal where H_2 is either injected (Thambimuthu et al. 2005; Oosterkamp and Ramsen, 2008) or produced in situ (Gallé, 2000; Ortiz et al., 2002).

Furthermore, given that pyrite is ubiquitous in natural geologic environments (Hall, 1986), as is the formation of natural H_2 in many geological settings (according to recent findings, e.g., Zgonnik, 2020; Boreham et al., 2021; Milkov, 2022; Truche et al., 2024), the abiotic reductive dissolution of pyrite may therefore be a more common alteration reaction than previously recognized. Hydrothermal systems with their characteristic black smokers at mid-ocean ridges, oceanic and continental crust exposed to H_2 produced by serpentinization, and the Archean prior to the Great Oxidation Event (Swanner et al., 2020; Zahnle et al., 2020) are examples for diverse anoxic, H_2-rich geologic environments throughout Earth's history where reductive pyrite alteration may have been important. These examples point out that aqueous pyrite-H_2 interactions, and in a more general sense aqueous H_2-driven reductive alteration of mineral phases, warrant further experimental and field studies.

Data availability

Data are available through Zenodo at https://doi.org/10.5281/zenodo.15877097.

CRediT authorship contribution statement

Robin Hintzen: Writing – review & editing, Writing – original draft, Visualization, Validation, Software, Methodology, Investigation, Funding acquisition, Formal analysis, Data curation, Conceptualization. **Roland Hellmann:** Writing – review & editing, Visualization, Validation, Supervision, Resources, Methodology, Investigation, Formal analysis, Conceptualization. **Vladimir Roddatis:** Writing – review & editing, Visualization, Validation, Methodology, Investigation, Formal analysis, Data curation. **Julia van Winden:** Conceptualization, Formal analysis, Methodology, Project administration, Resources, Software, Supervision, Validation, Writing – review & editing. **Laurent Truche:** Writing – review & editing, Validation, Supervision, Software, Resources, Project administration, Methodology, Investigation, Funding acquisition, Conceptualization.

Declaration of competing interest

The authors declare that they have no known competing financial interests or personal relationships that could have appeared to influence the work reported in this paper.

Acknowledgements

The authors acknowledge funding from Shell Global Solutions International B.V. and LT acknowledges support from the Institut Universitaire de France. This project has received additional funding from the European Union's Horizon 2020 research and innovation program under grant agreement No 101005611 for Transnational Access conducted at Helmholtz-Zentrum Potsdam Deutsches GeoForschungsZentrum (GFZ) as part of the Potsdam Imaging and Spectral Analysis (PISA) facility. The authors also thank the European Regional Development Fund and the State of Brandenburg for funding of the Themis Z microscope (part of the PISA facility) used in this work. In addition, the following contributions are highly acknowledged: P. De Rango (Inst. Néel) and E. Verloop (Inst. Néel) for support with the high

P_{H2} experiments, B. Lanson (ISTerre) and R. Martin (ISTerre) for help with XRD and SEM, A. Schreiber (GFZ) for the FIB specimen preparations for TEM, C. Ostertag-Henning (BGR), D. Daval (ISTerre, CNRS), J. Snippe (Shell), and E. Inan-Villegas (Shell) for valuable discussions. We also thank two anonymous reviewers for their constructive comments and C. Steefel for the editorial handling of this article.

Appendix A. Supplementary material

The supplementary material contains XRD patterns, SEM images of the unaltered pyrite powder (S.1), and additional information on the removal of native sulfur from the pyrite (S.2). The workflow of the PTMs is complemented by a graphical chart, the PHREEQC input file scripts, and PTM-related data tables for each experiment (S.3). An explanation of the uncertainty calculations is provided (S.4). Furthermore, an overview of each pyrite dissolution experiment is given that includes data tables and plots of the aqueous measurement data ($S^{-II}_{(aq)}$, pH, ICP-OES) on the one hand, and the Michaelis-Menten fits for the derivation of the pyrite dissolution rates at 12 hours on the other hand. The aqueous data also include all $S^{-II}_{(aq)}$ concentration measurements by methylene blue spectrophotometry, Ag^{+}/S^{-II} ion-selective electrode potentiometry, and ICP-OES as total elemental sulfur after H_2O_2-oxidation. In addition, some modeled data from the PTMs are compared with the measured data (corrected vs. modeled $pH_{in\ situ}$; measured vs. modeled dissolved Ca concentrations) (S.5). The alternative form of the rate equations based on Eq. (13) are developed (S.6). The performance of the kinetic rate laws (Eq. (23)) relative to the experimentally measured $S^{-II}_{(aq)}$ data is illustrated in concentration vs. time plots (S.7). The Michaelis-Menten fits over the complete experimental durations, including the data on the pyrite saturation index from the PTMs (SI_{FeS2}), that were used for the analysis of the r-ΔG_r relations, are summarized (S.8). Supplementary material to this article can be found online at https://doi.org/10.1016/j.gca.2025.12.034.

References

Aagaard, P., Helgeson, H.C., 1982. Thermodynamic and kinetic constraints on reaction rates among minerals and aqueous solutions I. Theoretical considerations. Am. J. Sci. 282, 237–285.
Bailey, L.K., Peters, E., 1976. Decomposition of pyrite in acids by pressure leaching and anodization: the case for an electrochemical mechanism. Can. Metall. Q. 15, 333–344.
Baird, R.B., Eaton, A.D., Rice, E.W., 2017. Standard methods for the examination of water and wastewater, twenty-third ed. American Public Health Association, Washington DC.
Beig, M.S., Lüttge, A., 2006. Albite dissolution kinetics as a function of distance from equilibrium: implications for natural feldspar weathering. Geochim. Cosmochim. Acta 70, 1402–1420.
Berner, R.A., 1978. Rate control of mineral dissolution under Earth surface conditions. Am. J. Sci. 278, 1235–1252.
Blanc, Ph., Lassin, A., Piantone, P., Azaroual, M., Jacquemet, N., Fabbri, A., Gaucher, E. C., 2012. Thermoddem: a geochemical database focused on low temperature water/rock interactions and waste materials. Appl. Geochem. 27, 2107–2116.
Bodunrin, M.O., Chown, L.H., Van Der Merwe, J.W., Alaneme, K.K., Oganbule, C., Klenam, D.E., Mphasha, N.P., 2020. Corrosion behavior of titanium alloys in acidic and saline media: Role of alloy design, passivation integrity, and electrolyte modification. Corros. Rev. 38, 25–47.
Boreham, C.J., Edwards, D.S., Czado, K., Rollet, N., Wang, L., van der Wielen, S., Champion, D., Blewett, R., Feitz, A., Henson, P.A., 2021. Hydrogen in Australian natural gas: occurrences, sources and resources. APPEA J. 61, 163–191.
Bourgeois, J.P., Aupaix, N., Bloise, R., Millet, J.L., 1979. Proposition d'explication de la formation d'hydrogène sulfure dans les stockages souterrains de gaz naturel par réduction des sulfures minéraux de la roche magasin. Revue De L'institut Français Du Pétrole 34, 371–386.
Braid, H., Taylor, K., Hough, E., Rochelle, C., Niasar, V., Ma, L., 2024. Hydrogen-induced mineral alteration: a review in the context of underground hydrogen storage (UHS) in saline aquifers. Earth Sci. Rev. 259, 104975.
Butler, I.B., Schoonen, M.A.A., Rickard, D.T., 1994. Removal of dissolved oxygen from water: a comparison of four common techniques. Talanta 41, 211–215.
Burch, T.E., Nagy, K.L., Lasaga, A.C., 1993. Free energy dependence of albite dissolution kinetics at 80 °C and pH 8.8. Chem. Geol. 105, 137–162.
Cama, J., Ayora, C., Lasaga, A.C., 1999. The deviation-from-equilibrium effect on dissolution rate and on apparent variations in activation energy. Geochim. Cosmochim. Acta 63, 2481–2486.
Carroll, S.A., Walther, J.V., 1990. Kaolinite dissolution at 25°, 60°, and 80°C. Am. J. Sci. 290, 797–810.
Casey, W.H., Sposito, G., 1992. On the temperature dependence of mineral dissolution rates. Geochim. Cosmochim. Acta 56, 3825–3830.
Chandra, A.P., Gerson, A.R., 2010. The mechanisms of pyrite oxidation and leaching: a fundamental perspective. Surf. Sci. Rep. 65, 293–315.
Chiriță, P., Schlegel, M.L., 2017. Pyrite oxidation in air-equilibrated solutions: an electrochemical study. Chem. Geol. 470, 67–74.
Cline, J.D., 1969. Spectrophotometric determination of hydrogen sulfide in natural waters. Limnol. Oceanogr. 14, 454–458.
Crerar, D.A., Susak, N.J., Borcsik, M., 1978. Solubility of the buffer assemblage pyrite + pyrrhotite + magnetite in NaCl solutions from 200 to 350°C. Geochim. Cosmochim. Acta 42, 1427–1437.
Doebelin, N., Kleeberg, R., 2015. Profex: a graphical user interface for the Rietveld refinement program BGMN. J. Appl. Cryst. 48, 1573–1580.
Domènech, C., de Pablo, J., Ayora, C., 2002. Oxidative dissolution of pyritic sludge from the Aznalcóllar mine (SW Spain). Chem. Geol. 190, 339–353.
Dove, P.M., Han, N., De Yoreo, J.J., 2005. Mechanisms of classical crystal growth theory explain quartz and silicate dissolution behavior. Proc. Nat. Acad. Sci. 102, 15357–15362.
Evangelou, V.P.B., Zhang, Y.L., 2009. A review: Pyrite oxidation mechanisms and acid mine drainage prevention. Crit. Rev. Environ. Sci. Technol. 25, 141–199.
Feng, J., Tian, H., Huang, Y., Ding, Z., Yin, Z., 2019. Pyrite oxidation mechanism in aqueous medium. J. Chin. Chem. Soc. 66, 345–354.
Fishman, M.J., Friedman, L.C., 1989. Methods for determination of inorganic substances in water and fluvial sediments, third ed. United States Government Printing Office, Washington.
Gallé, C., 2000. Gas breakthrough pressure in compacted Fo-Ca clay and interfacial gas overpressure in waste disposal context. Appl. Clay Sci. 17, 85–97.
Golubev, S.V., Bauer, A., Pokrovsky, O.S., 2006. Effect of pH and organic ligands on the kinetics of smectite dissolution at 25 °C. Geochim. Cosmochim. Acta 70, 4436–4451.
Hall, A.J., 1986. Pyrite-pyrrhotine redox reactions in nature. Mineral. Mag. 50, 223–229.
Hassannayebi, N., Azizmohammadi, S., De Lucia, M., Ott, H., 2019. Underground hydrogen storage: application of geochemical modelling in a case study in the Molasse Basin Upper Austria. Environ. Earth Sci. 78, 177.
Heinemann, N., Alcalde, J., Miocic, J.M., Hangx, S.J.T., Kallmeyer, J., Ostertag-Henning, C., Hassanpouryouzband, A., Thaysen, E.M., Strobel, G.J., Schmidt-Hattenberger, C., Edlmann, K., Wilkinson, M., Bentham, M., Haszeldine, R.S., Carbonell, R., Rudloff, A., 2021. Enabling large-scale hydrogen storage in porous media – the scientific challenges. Energy Environ. Sci. 14, 853–864.
Hellmann, R., 1994. The albite-water system: Part I. The kinetics of dissolution as a function of pH at 100, 200, and 300 °C. Geochim. Cosmochim. Acta 58, 595–611.
Hellmann, R., Tisserand, D., 2006. Dissolution kinetics as a function of the Gibbs free energy of reaction: an experimental study based on albite feldspar. Geochim. Cosmochim. Acta 70, 364–383.
Hellmann, R., Daval, D., Tisserand, D., 2010. The dependence of albite feldspar dissolution kinetics on fluid saturation state at acid and basic pH: progress towards a universal relation. C. R. Geosc. 342, 676–684.
Hendrix, K., Bleyen, N., Mennecart, T., Gaigneaux, E.M., Eloy, P., Valcke, E., 2022. Surface-mediated redox activity in the pyrite - nitrate/nitrite - hydrogen system under conditions relevant for the geological disposal of bituminized waste in Boom Clay. Appl. Geochem. 143, 105386.
Hoffmann, M.R., 1977. Kinetics and mechanism of oxidation of hydrogen sulfide by hydrogen peroxide in acidic solution. Environ. Sci. Technol. 11, 61–66.
Holmes, P.R., Crundwell, F.K., 2000. The kinetics of the oxidation of pyrite by ferric ions and dissolved oxygen: an electrochemical study. Geochim. Cosmochim. Acta 64, 263–274.
International Association for the Properties of Water and Steam (IAPWS), 2019. Revised Release on the Ionization Constant of H_2O, R11-07.
Jay, S., Cézac, P., Serin, J.-P., Contamine, F., Martin, C., Mercadier, J., 2009. Solubility of elemental sulfur in toluene between (267.15 and 313.15) K under atmospheric pressure. J. Chem. Eng. Data 54, 3238–3241.
Johnson, A.C., Romaniello, S.J., Reinhard, C.T., Gregory, D.D., Garcia-Robledo, E., Revsbech, N.P., Canfield, D.E., Lyons, T.W., Anbar, A.D., 2019. Experimental determination of pyrite and molybdenite oxidation kinetics at nanomolar oxygen concentrations. Geochim. Cosmochim. Acta 249, 160–172.
Kishima, N., 1989. A thermodynamic study on the pyrite-pyrrhotite-magnetite-water system at 300-500°C with relevance to the fugacity / concentration quotient of aqueous H_2S. Geochim. Cosmochim. Acta 53, 2143–2155.
Knauss, K.G., Wolery, T.J., 1989. Muscovite dissolution kinetics as a function of pH and time at 70 °C. Geochim. Cosmochim. Acta 53, 1493–1501.
Köhler, S.J., Dufaud, F., Oelkers, E.H., 2003. An experimental study of illite dissolution kinetics as a function of pH from 1.4 to 12.4 and termperature from 5 to 50°C. Geochim. Cosmochim. Acta 67, 3583–3594.
Labus, K., Tarkowski, R., 2022. Modeling hydrogen – rock – brine interactions for the Jurassic reservoir and cap rocks from Polish Lowlands. Int. J. Hydrog. Energy 47, 10947–10962.
Lambert, J.M., Simkovich Jr., G., Walker Jr., P.L., 1998. The kinetics and mechanism of the pyrite-to-pyrrhotite transformation. Metall. Mater. Trans. B 29, 385–396.
Lasaga, A.C., 1981. Transition state theory, in: Lasaga, A.C., Kirkpatrick, R.J. (Eds.), Kinetics of Geochemical Processes. Mineralogical Society of America, pp. 135-169.
Lasaga, A.C., 1984. Chemical kinetics of water-rock interactions. J. Geophys. Res. 89, 4009–4025.
Lasaga, A.C., Gibbs, G.V., 1990. Ab-initio quantum mechanical calculations of water-rock interactions: adsorption and hydrolysis reactions. Am. J. Sci. 290, 263–295.

Lasaga, A.C., 1995. Fundamental approaches in describing mineral dissolution and precipitation rates, in: White, A.F., Brantley, S.L. (Eds.), Chemical Weathering Rates of Silicate Minerals. Mineralogical Society of America, pp. 23-86.
Lasaga, A.C., 1998. Kinetic theory in the Earth sciences. Princeton University Press, New Jersey.
Lasaga, A.C., Lüttge, A., 2001. Variation of crystal dissolution rate based on a dissolution stepwave model. Science 291, 2400–2404.
Lasaga, A.C., Lüttge, A., 2004. Mineralogical approaches to fundamental crystal dissolution kinetics - dissolution of an A_3B structure. Eur. J. Miner. 16, 713–729.
Lawrence, N.S., Davis, J., Compton, R.G., 2000. Analytical strategies for the detection of sulfide: a review. Talanta 52, 771–784.
Lennie, A.R., Vaughan, D.J., 1996. Spectroscopic studies of iron sulfide formation and phase relations at low temperatures. In: Dyar, M.D., McCammon, C., Schaefer, M.W. (Eds.), Mineral Spectroscopy: A Tribute to Roger g. Burns. The Geochemical Society, No. 5. Special Publication, pp. 117–131.
Li, Y., Peng, Y., Wei, Z., Yang, X., Gerson, A.R., 2023. Crystal face-dependent pyrite oxidation: an electrochemical study. Appl. Surf. Sci. 619, 156687.
Liu, J., Yang, T., Peng, Q., Yang, Y., Li, Y.W., Wen, X.-D., 2021. Theoretical exploration of the interaction between hydrogen and pyrite-type FeS_2 surfaces. Appl. Surf. Sci. 537, 147900.
Lüttge, A., 2006. Crystal dissolution kinetics and Gibbs free energy. J. Electron Spectrosc. Relat. Phenom. 150, 248–259.
Lüttge, A., Arvidson, R.S., Fischer, C., Kurganskaya, I., 2019. Kinetic concepts for quantitative prediction of fluid-solid interactions. Chem. Geol. 504, 216–235.
Mandeville, C.W., 2010. Sulfur: a ubiquitous and useful tracer in earth and planetary sciences. Elements 6, 75–80.
Marty, N.C.M., Claret, F., Lassin, A., Tremosa, J., Blanc, P., Madé, B., Giffaut, E., Cochepin, B., Tournassat, C., 2015. A database of dissolution and precipitation rates for clay-rocks minerals. Appl. Geochem. 55, 108–118.
Mathews, C.T., Robins, R.G., 1974. Aqueous oxidation of iron disulfide by molecular oxygen. Australian Chem. Eng. 15, 19–24.
McKibben, M., Barnes, H.L., 1986. Oxidation of pyrite in low temperature acidic solution: rate laws and surface textures. Geochim. Cosmochim. Acta 50, 1509–1520.
Mettler Toledo, 2011. PerfectION^{TM} Guidebook: Combination silver/sulfide electrode. https://www.mt.com/us/en/home/library/operating-instructions/lab-analytical-instruments/GB_SilverSulf.html (accessed 14 February 2025).
Milkov, A.V., 2022. Molecular hydrogen in surface and subsurface natural gases: abundance, origins and ideas for deliberate exploration. Earth-Sci. Rev. 230, 104063.
Millero, F.J., LeFerrier, A., Fernandez, M., Hubinger, S., Hershey, J.P., 1989. Oxidation of hydrogen sulfide with hydrogen peroxide in natural waters. Environ. Sci. Technol. 23, 209–213.
Moses, C.O., Nordstrom, D.K., Herman, J.S., Mills, A.L., 1987. Aqueous pyrite oxidation by dissolved oxygen and by ferric iron. Geochim. Cosmochim. Acta 51, 1561–1571.
Nagy, K.L., Lasaga, A.C., 1992. Dissolution and precipitation kinetics of gibbsite at 80 °C and pH 3: the dependence on solution saturation state. Geochim. Cosmochim. Acta 56, 3093–3111.
Nordstrom, D.K., 1982. Aqueous pyrite oxidation and the consequent formation of secondary iron minerals. In: Kittrick, A., Fanning, D.S., Hossner, L.R. (Eds.), Acid Sulfate Weathering. Soil Science Society of America Inc., Madison, pp. 37–56.
Oelkers, E.H., 2001. General kinetic description of multioxide silicate mineral and glass dissolution. Geochim. Cosmochim. Acta 65, 3703–3719.
Oosterkamp, A., Ramsen, J., 2008. State-of-the-art overview of CO_2 pipeline transport with relevance to offshore pipelines. Polytec, POL-O-2007-138-A, pp. 87.
Ortiz, L., Volckaert, G., Mallants, D., 2002. Gas generation and migration in Boom Clay, a potential host rock formation for nuclear waste storage. Eng. Geol. 64, 287–296.
Overwijk, M.H.F., van den Heuvel, F.C., Bulle-Lieuwma, C.W.T., 1993. Novel scheme for the preparation of transmission electron microscopy specimens with a focused ion beam. J. Vac. Sci. Technol. 11, 2021–2024.
Parkhurst, D.L., Appelo, C.A.J., 2013. Description of input and examples for PHREEQC version 3: a computer program for speciation, batch-reaction, one-dimensional transport, and inverse geochemical calculations. US Geological Survey 6–A43.
Pokrovsky, O.S., Golubev, S.V., Schott, J., 2005. Dissolution kinetics of calcite, dolomite and magnesite at 25 °C, and 0 to 50 atm pCO_2. Chem. Geol. 217, 239–255.
Rauscher, A., Kutsan, G., Lukacs, Z., 1990. Effects of hydrogen sulphide and temperature on passivation behaviour of titanium. Corros. Sci. 31, 255–260.
Reese, B.K., Finneran, D.W., Mills, H.J., Zhu, M.-X., Morse, J.W., 2011. Examination and refinement of the determination of aqueous hydrogen sulfide by the methylene blue method. Aquat. Geochem. 17, 567–582.
Reitenbach, V., Ganzer, L., Albrecht, D., Hagemann, B., 2015. Influence of added hydrogen on underground gas storage: a review of key issues. Environ. Earth Sci. 73, 6927–6937.
Rickard, D., Luther, G.W., 1997. Kinetics of pyrite formation by the H_2S oxidation of iron (II) monosulfide in aqueous solutions between 25 and 125°C: The mechanism. Geochim. Cosmochim. Acta 61, 135–147.
Rickard, D., Luther, G.W., 2007. Chemistry of iron sulfides. Chem. Rev. 107, 514–562.
Rozalén, M., Brady, P.V., Huertasm, F.J., 2009. Surface chemistry of K-montmorillonite: ionic strength, temperature dependence and dissolution kinetics. J. Colloid Interface Sci. 333, 474–484.
Schott, J., Pokrovsky, O.S., Oelkers, E.H., 2009. The link between mineral dissolution/precipitation kinetics and solution chemistry, in: Oelkers, E.H., Schott, J. (Eds.), Thermodynamics and Kinetics of Water-Rock Interaction. Mineralogical Society of America, pp. 207-258.
Seewald, J.S., Zolotoc, M.Y., McCollom, T., 2006. Experimental investigation of single carbon compounds under hydrothermal conditions. Geochim. Cosmochim. Acta 70, 446–460.
Steefel, C.I., 2009. CrunchFlow. Software for modeling multicomponent reactive flow and transport. User's manual. Lawrence Berkeley National Laboratory. https://www.netl.doe.gov/sites/default/files/netl-file/CrunchFlow-Manual.pdf (accessed 21 June 2025).
Swanner, E.D., Lambrecht, N., Wittkop, C., Harding, C., Katsev, S., Torgeson, J., Poulton, S.W., 2020. The biogeochemistry of ferruginous lakes and past ferruginous oceans. Earth-Sci. Rev. 211, 103430.
Taylor, A.S., Blum, J.D., Lasaga, A.C., 2000. The dependence of labradorite dissolution and Sr isotope release rates on solution saturation state. Geochim. Cosmochim. Acta 64, 2389–2400.
Thambimuthu, K.K., Soltanieh, M., Abanades, J.C., 2005. Capture of CO2. In: Mettz, B., Davidson, O., de Coninck, H., Loos, M., Meyer, L. (Eds.), IPCC Special Report on Carbon Dioxide Capture and Storage. Cambridge University Press, Cambridge, pp. 105–178.
Titanium Metals Corporation, 1997. Corrosion resistance of titanium. https://www.timet.com/assets/local/documents/technicalmanuals/corrosion.pdf (accesses 21 June 2025).
Truche, L., Berger, G., Destrigneville, C., Guillaume, D., Giffaut, E., 2010. Kinetics of pyrite to pyrrhotite reduction by hydrogen in calcite buffered solutions between 90 and 180 °C: Implications for nuclear waste disposal. Geochim. Cosmochim. Acta 74, 2894–2914.
Truche, L., Jodin-Caumon, M.-C., Lerouge, C., Berger, G., Mosser-Ruck, R., Giffaut, E., Michau, N., 2013. Sulphide mineral reactions in clay-rich rock induced by high hydrogen pressure. Application to disturbed or natural settings up to 250 °C and 30 bar. Chem. Geol. 351, 217–228.
Truche, L., Donzé, F.-V., Goskolli, E., Muceku, B., Loisy, C., Monnin, C., Dutoit, H., Cerepi, A., 2024. A deep reservoir for hydrogen drives intense degassing in the Bulqizë ophiolite. Science 383, 618–621.
Vialle, S., Wolff-Boenisch, D., 2024. Thermodynamic and kinetic considerations of the link between underground hydrogen storage and reductive carbonate dissolution and methane production. Are limestone reservoirs unsuitable for UHS? Chem. Geol. 665, 122304.
Williamson, M.A., Rimstidt, J.D., 1994. The kinetics and electrochemical rate-determining step of aqueous pyrite oxidation. Geochim. Cosmochim. Acta 58, 5443–5454.
Xu, T., Sonnenthal, E., Spycher, N., Pruess, K., 2006. Toughreact-a simulation program for non-isothermal multiphase reactive geochemical transport in variably saturated geologic media: applications to geothermal injectivity and CO_2 geological sequestration. Comput. Geosci. 32, 145–165.
Xu, T., Spycher, N., Sonnenthal, E., Zhang, G., Zheng, L., Pruess, K., 2011. Toughreact version 2.0: a simulator for subsurface reactive trnasport under non-isothermal multiphase flow conditions. Comput. Geosci. 37, 763–774.
Zahnle, K.J., Lupu, R., Catling, D.C., Wogan, N., 2020. Creation and evolution of impact-generated reduced atmospheres of Early Earth. Planet. Sci. J. 1 (1), 11.
Zekos, I., Stack, M.M., 2019. A note on a design protocol for deoxygenation of water. Electrochem. Commun. 103, 12–16.
Zgonnik, V., 2020. The occurrence and geoscience of natural hydrogen: a comprehensive review. Earth-Sci. Rev. 203, 103140.
Zhu, Y., Heo, T.W., Rodriguez, J.N., Weber, P.K., Shi, R., Baer, B.J., Morgado, F.F., Antonov, S., Kweon, K.E., Watkins, E.B., Savage, D.J., Chapman, J.E., Keilbart, N.D., Song, Y., Zhen, Q., Gault, B., Vogel, S.C., Sen-Britain, S.T., Shalloo, M.G., Orme, C., Bagge-Hansen, M., Hahn, C., Pham, T.A., MacDonald, D.D., Qiu, S.R., Wood, B.C., 2022. Hydriding of titanium: recent trends and perspectives in advanced characterization and multiscale modeling. Curr. Opin. Solid State Mater. Sci. 26, 101020.
Zivar, D., Kumar, S., Foroozesh, J., 2021. Underground hydrogen storage: a comprehensive review. Int. J. Hydrog. Energy 46, 23436–23462.